POLITECNICO DI TORINO
Repository ISTITUZIONALE

VED-dependent HIP densification of PBF-LB Inconel 718: Defect closure thresholds, microstructural homogenization, and nano-mechanical response

Original
VED-dependent HIP densification of PBF-LB Inconel 718: Defect closure thresholds, microstructural homogenization, and nano-mechanical response / Anwar, J., Bassini, E., Cannella, M., Marchese, G., Martucci, A., Biamino, S., Lombardi, M., Ugues, D.. - In: JOURNAL OF ALLOYS AND COMPOUNDS. - ISSN 0925-8388. - ELETTRONICO. - 1082:(2026), pp. 1-17. [10.1016/j.jallcom.2026.191395]

Availability:
This version is available at: 11583/3016247 since: 2026-10-02T20:02:56Z

Publisher:
Elsevier

Published
DOI:10.1016/j.jallcom.2026.191395

Terms of use:

This article is made available under terms and conditions as specified in the corresponding bibliographic description in the repository

Publisher copyright

(Article begins on next page)

06 November 2026

Journal of Alloys and Compounds 1082 (2026) 191395

Contents lists available at ScienceDirect

Journal of Alloys and Compounds

journal homepage: www.elsevier.com/locate/jalcom

VED-dependent HIP densification of PBF-LB Inconel 718: Defect closure thresholds, microstructural homogenization, and nano-mechanical response

Jehanzaib Anwar [a], Emilio Bassini [b,*], Mattia Cannella [a], Giulio Marchese [a], Alessandra Martucci [a], Sara Biamino [a], Mariangela Lombardi [a], Daniele Ugues [a]

[a] Politecnico di Torino Dipartimento Scienza Applicata e Tecnologia, Italy
[b] Politecnico di Torino, Department of applied Science and Technology, Corso Duca degli Abruzzi, 24, 10129 Torino, Italy

ARTICLE INFO

Keywords:
Laser powder bed fusion
Inconel 718
Volumetric energy density
Hot isostatic pressing
HIP densification efficiency
Porosity threshold
Microstructural homogenization

ABSTRACT

Defining the initial porosity limits within which hot isostatic pressing (HIP) can effectively densify laser powder bed fusion (PBF-LB) components remains a critical gap for industrial qualification of additively manufactured nickel-based superalloys. This study systematically investigates the influence of volumetric energy density (VED) on initial defect population in Inconel 718 (IN718) and its role in densification response during HIP. Specimens with varying initial porosity (0.01–17.76%) were fabricated by intentionally varying laser power, scan speed, and hatch spacing. All samples were subjected to identical HIP conditions (1160 °C, 100 MPa, 4 h) incorporating a combined in-situ solution treatment, followed by double ageing in a vacuum furnace. Porosity evolution, pore morphology, microstructural transformations, and nano-mechanical response were characterized before and after HIP. Three distinct densification regimes were identified based on initial porosity. Below 0.1%, the absolute densification benefit is negligible due to argon-filled gas pores resistant to closure. Between 0.1% and 10%, closure efficiencies of 87–98% are achieved, representing the optimal HIP densification window. Between 10% and 17%, the response degrades progressively, and above ~17% densification efficiency becomes negative owing to open-pore network formation and argon gas expansion during subsequent vacuum treatments. Furthermore, HIP at 1160 °C fully dissolved Nb-rich laves phases, eliminated melt pool boundaries, and promoted recrystallization from columnar to equiaxed grain structure. Double ageing produced a uniform distribution of fine γ'/γ'' strengthening precipitates. These findings establish quantitative defect acceptance criteria for pre-HIP qualification of PBF-LB nickel superalloy components, supporting cost-effective post-processing for aerospace and energy applications.

1. Introduction

Metal additive manufacturing (AM) has gained significant attention in recent decades due to its excellent ability to fabricate complex near-net-shape components directly from digital models, reducing material waste and steps as compared to other manufacturing processes [1]. Among these AM processes, laser powder bed fusion (PBF-LB), also known as selective laser melting (SLM), has emerged as a promising candidate for producing high-performance metallic components with high geometric resolution, relative density, and control over the part produced, particularly required in aerospace and energy applications where performance optimization is critical, i.e., nickel based super alloys used at high temperature areas [2,3]. Despite the multiple advantages of PBF-LB, the process involves rapid melting and solidification, which may lead to microstructural heterogeneity, residual stress, and the formation of internal defects. These defects are usually classified as gas pores, keyhole pores, and lack-of-fusion (LOF) voids, each with unique formation mechanisms and shapes; LOF defects are generally the most crack-like and damaging in fatigue because of sharp internal notches and unmelted interfaces [4].

Moreover, defects are also highly dependent on the PBF-LB processing parameters, particularly laser power, scanning speed, hatch spacing, and layer thickness, which collectively contribute to the applied energy density (VED) to the powder. An increase in VED can lead to

* Corresponding author.
E-mail address: emilio.bassini@polito.it (E. Bassini).

https://doi.org/10.1016/j.jallcom.2026.191395
Received 11 August 2026; Received in revised form 18 September 2026; Accepted 27 September 2026
Available online 1 October 2026
0925-8388/© 2026 The Authors. Published by Elsevier B.V. This is an open access article under the CC BY-NC-ND license (http://creativecommons.org/licenses/by-nc-nd/4.0/).

excessive melt pool instability, keyhole formation, vaporization-induced porosity, and, in extreme cases, localized burn-through. Conversely, a reduction results in incomplete melting, poor interlayer bonding, irregular melt pool morphology, and lack-of-fusion defects and irregular porosity. Furthermore, raw material, i.e., powders, also has a critical role, including entrapped gas, irregular particle morphology, flowability, and powder reuse, which can influence the final properties of the produced parts [5,6]. In addition, variations in powder spreading and scan strategy may promote discontinuous melt tracks, thereby increasing the susceptibility to pore formation. These defects can significantly degrade mechanical performance by acting as stress concentrators and crack initiation sites, thereby failing to meet the stringent requirements of aerospace and energy applications.

Among various nickel-based superalloys, Inconel 718 (IN718) has recently gained significant attention for manufacturing via the PBF-LB process due to its excellent weldability, while maintaining excellent high-temperature mechanical properties, making it an ideal candidate for additive manufacturing to produce complex parts for aerospace and energy applications [7]. This superior mechanical performance of IN718 is due to the formation of coherent γ' (Ni_3 (Al, Ti)) and γ'' (Ni_3 Nb) precipitates, strengthening the γ matrix. However, among these precipitates, γ'' is the primary strengthening agent, reducing the susceptibility to solidification cracking during rapid melting and solidification due to a narrower solidification temperature range and more ductile interdendritic regions during rapid solidification, thereby making it more suitable for additive manufacturing processes. Consequently, this alloy is extensively employed in gas turbine engines and other high-temperature structural applications where complexity, along with high mechanical properties are essential. Despite these advantages, PBF-LB manufactured IN718 exhibits inherent AM process-induced defects, as discussed above. Along with these defects, anisotropy and microstructural segregation due to rapid solidification are also challenges that can negatively influence the overall mechanical response and structural integrity of the part, which needs attention when dealing with AM-manufactured parts [8].

Multiple studies were conducted to reduce the anisotropy in the AM parts by controlling the manufacturing parameters or by post-heat-treating the AM parts [9,10]. However, the porosity issue remains unresolved and, in some cases, increases after the heat treatments. To mitigate both issues in a single-step post-processing treatment, hot isostatic pressing (HIP) has been widely investigated and proven as an effective technique in reducing internal porosity and also improving microstructural isotropy. In this process, high temperature and isostatic pressure are simultaneously applied to the material with the help of gas, promoting diffusion, plastic deformation, and pore shrinkage, thereby increasing the relative density of metallic components to the near theoretical density [11]. Traditionally, HIP has been employed in cast superalloys to eliminate shrinkage porosity and reduce segregation, leading to improvements in tensile strength, ductility, and fatigue life. Chang et al. [12] working on cast IN718 superalloy, reported that HIP at approximately 1180 °C significantly reduced segregation and internal porosity while increasing room-temperature tensile strength by 18% and elongation by more than 50%. Similar benefits have been reported for additively manufactured components, where HIP treatment mitigates these inherent drawbacks of the AM process.

Previous studies on PBF-LB IN718 have demonstrated that HIP as an effective post-processing technique for improving densification and microstructural homogeneity. For example, Yin et al. [13] evaluated the effects of HIP on PBF-LB IN718 at multiple temperatures, ranging from 1120 to 1180 °C, followed by solution and ageing heat treatments, on the microstructure and tensile properties. It was observed that HIP temperatures dissolve the laves phases produced in the as-built part and promote grain recrystallization. This dissolution is expected on thermodynamic grounds: in the as-built condition, rapid solidification drives extensive Nb segregation into the interdendritic regions, where it combines with Ni, Fe and Cr to form the metastable Laves phase, which dissolves readily above approximately 1050 °C [14], returning Nb to solid solution and enabling subsequent precipitation of the primary strengthening phase γ'' (Ni_3Nb, $D0_{22}$ structure) and the secondary γ' phase ($Ni_3(Al,Ti)$, $L1_2$ structure) during ageing. The Nb released by this dissolution does not remain entirely in solution, however: cooling from the HIP temperature and through any subsequent solution treatment, some of this Nb instead reforms as needle-like δ-phase (Ni_3Nb, $D0_a$ structure) at grain and twin boundaries, favored by the locally higher Nb activity at these interfaces [15], together with blocky MC carbides that remain stable up to the melting point [16]. The δ-phase plays a dual role in this context: moderate amounts pin grain boundaries and restrict grain growth during the high-temperature hold, but once its volume fraction exceeds approximately 4–8%, it depletes the matrix of Nb available for γ'' formation and acts as a stress raiser owing to its acicular morphology, degrading both strength and ductility [17]. This recrystallization behavior strongly depends on the HIP temperature, with fully equiaxed grains observed at temperatures $\geq$ 1150 °C. However, an increase in HIP temperature results in grain coarsening, along with a strength and ductility trade-off in mechanical properties. Similarly, Varela et al. [18] also examined the effect of HIP on PBF-LB IN718 at 1105–1200 °C, and observed the formation of equiaxed recrystallized grains. Comparable observations were also reported by Sommer et al. [19], in which improvement in mechanical properties was observed due to varying post-processing routes in PBF-LB IN718. Two routes were examined, one with HIP, along with stress-relief (SR) heat treatment and double ageing (DA), and the other without HIP. First process improved microstructural homogenization and density, in contrast to the second route, resulting in increased tensile strength from 849 to 1155 MPa and fatigue strength to 190 MPa compared to 85 MPa in the as-built sample. This increased mechanical response was due to reduced defects and homogenization of the microstructure, leading to uniform crack initiation.

Although HIP is effective in improving densification, its success is not universal but governed by the characteristics of the initial defect population, namely pore size, morphology, and entrapped gas content. From a thermodynamic perspective, closure of a spherical pore of radius r requires that the applied pressure overcomes both the internal gas pressure and the resistance associated with the pore surface [20]:

$$Pext \quad > Pint + \frac{2\gamma}{r} \tag{1}$$

where P_ext is the applied HIP pressure, P_int is the internal gas pressure, and $2\gamma/r$ is the surface-energy contribution. Since the latter scales inversely with pore radius, fine pores are intrinsically more resistant to closure than large lack-of-fusion defects, while the internal pressure term is set by the nature of the entrapped gas. Nitrogen-filled pores, originating from atmospheric or powder contamination, are relatively amenable to closure through dissolution of the gas into the matrix, whereas argon is essentially insoluble in the Ni–Fe–Cr lattice and therefore resists complete elimination regardless of applied pressure and temperature [21,22]. These considerations, together with the cost of the process itself, define the thresholds that must be assessed when evaluating whether HIP is justified for a given component [11]. In the work of Tillmann et al. [23] performed on PBF-LB IN718, it was demonstrated via micro-CT and microscopy that HIP substantially densifies PBF-LB IN718, reducing porosity from 0.069 to 0.011–0.015 vol% at temperatures $\geq$ 1150 °C and pressures $\geq$ 100 MPa, and down to ~0.0019%. Their parametric analysis indicated that temperature is the dominant densification driver, as limited improvement was observed below 900 °C and near-saturation above 1150 °C, leading them to identify 1150 °C with a pressure of 100 MPa as an economical condition for HIP IN718. Nevertheless, isolated micron-scale pores persisted after HIP, which they attributed to entrapped argon gas, indicating that gas-filled porosity cannot be fully healed by HIP alone. Other studies have also reported similar results, where HIP improved density, hardness, and fatigue

resistance primarily through closure of shrinkage and lack-of-fusion defects rather than complete elimination of gas porosity [24]. Kaletsch et al. [22] investigated whether PBF-LB productivity for IN 718 can be increased by intentionally printing parts with high porosity and then densifying them using HIP. Samples with about 3.5% and 9.9% core porosity were HIP-treated and then aged with and without pressure conditions. For the lower porosity, HIP produced high fatigue strength regardless of the ageing condition, but for the high porosity case, a notable difference was observed. Specimens aged under pressure retained high fatigue strength, while those aged without pressure showed a drastic reduction due to the trapped argon gas that expands, causing pore regrowth and separation along weak interfaces, reducing bonding. Although the fatigue behavior clearly indicates this mechanism, the study could not quantitatively measure the pore regrowth. Similarly, other studies have also recently reported that HIP cannot heal surface-opening cracks in nickel superalloys and can even extend them, and also, subsequent heat treatment after HIP can re-enlarge pores due to trapped-gas expansion [25,26].

Despite the mentioned studies, a fundamental gap remains, where no study has systematically characterized HIP densification efficiency as a continuous function of initial porosity across a range wide enough to capture the transition from gas-pore-dominated to LOF-dominated to open-pore-network regimes, as per the best of the author's knowledge. Existing studies either examine near-fully dense PBF-LB material where HIP benefit is marginal or intentionally introduce high porosity without quantifying the precise threshold beyond which HIP becomes ineffective. Specifically, the mechanism by which argon gas entrapment during PBF-LB has been observed qualitatively but never quantified in terms of a porosity acceptance limit. This absence of quantitative threshold data represents a direct barrier to industrial qualification, where component acceptance criteria must be defined before HIP.

The present study addresses these gaps by fabricating a matrix of 30 PBF-LB IN718 specimens spanning nearly three orders of magnitude in initial porosity (0.01–17.76%), subjecting all samples to identical HIP conditions incorporating a combined solution treatment cycle, and systematically characterizing defect evolution, pore morphology, microstructural transformation, crystallographic texture, and mechanical response before and after processing. Specifically, this work establishes quantitative porosity thresholds that define the effective operating window for HIP densification, identifies the mechanisms responsible for HIP inefficiency at both low and high initial porosity extremes, and links defect closure behavior to microstructural evolution and mechanical response. These findings provide evidence-based acceptance criteria for pre-HIP qualification of PBF-LB nickel superalloy components, supporting cost-effective post-processing for aerospace and energy applications.

2. Materials and methods

2.1. Material and PBF-LB fabrication

Gas-atomized IN718 was used as feedstock material. The powder consisted of predominantly spherical particles produced by gas atomization, with a particle size distribution ranging between 20 and 55 μm, suitable for PBF-LB processing.

A total of thirty cubic specimens with dimensions of $10 \times 10 \times 10$ mm^3 were fabricated using an PBF-LB system manufactured by TRUMPF TruPrint 1000 operating under an argon atmosphere, as tabulated in Table 1. To intentionally generate different initial porosity levels, the PBF-LB processing parameters were systematically varied by modifying laser power, scan speed, and hatch spacing, resulting in different volumetric energy densities. The reported volumetric energy density values are calculated as per the following equation:

Table 1
PBF-LB samples parameters.

Sample no.	Energy density (J/mm3)	Laser Power (W)	Hatch distance (mm)	Scan Speed (mm/s)
1	111	100	0.05	900
2	83	100	0.05	1200
3	67	100	0.05	1500
4	79	100	0.07	900
5	60	100	0.07	1200
6	48	100	0.07	1500
7	62	100	0.09	900
8	46	100	0.09	1200
9	37	100	0.09	1500
10	167	150	0.05	900
11	125	150	0.05	1200
12	100	150	0.05	1500
13	119	150	0.07	900
14	89	150	0.07	1200
15	71	150	0.07	1500
16	93	150	0.09	900
17	69	150	0.09	1200
18	56	150	0.09	1500
19	222	200	0.05	900
20	167	200	0.05	1200
21	133	200	0.05	1500
22	159	200	0.07	900
23	119	200	0.07	1200
24	95	200	0.07	1500
25	123	200	0.09	900
26	93	200	0.09	1200
27	74	200	0.09	1500
28	37	100	0.09	1500
29	93	200	0.09	1200
30	222	200	0.05	900

$$E_v = \frac{P}{(v * h * t)} \quad (2)$$

Where P is laser power (W), v is the scan speed (mm/s), and h is the hatch distance (mm). The layer thickness appears to have been held constant at 20 μm. This approach enabled the production of samples with controlled variations in defect content, including both spherical gas pores and irregular lack-of-fusion defects arising from insufficient melting conditions. All specimens were fabricated with the same laser spot size of 50 μm and a scan rotation between layers of 67°.

After fabrication, the samples were removed from the built platform using wire electrical discharge machining. No stress-relief treatment was applied prior to hot isostatic pressing to preserve the as-built porosity for densification analysis.

2.2. Hot isostatic pressing and heat treatment

HIP was carried out using a HIP system of Quintus technology model QIH 15 L at 1160 °C under 100 MPa for 4 h, along with solution treatment at 980 °C for 1 h under pressure with high-purity argon as the pressure-transmitting medium, as per already optimized parameters [27,28]. This single-step HIP + solutionizing treatment will not only save the energy wasted during the separate solutionizing heating cycle but also save time, ultimately improving the efficiency of the system. This result was achieved thanks to the hip-quench capability of the press; ca. 120 °C/min was the cooling rate adopted after the solutioning stage. Subsequently, double ageing was performed using a vacuum furnace (102 mbar), TAV MINIJET HP S/N 235, at 720 °C and 620 ∘C for 8 h at each temperature, as depicted in Fig. 1. This two-step ageing treatment promotes the precipitation of γ' and γ'' strengthening phases within the γ matrix, which are responsible for the high strength of IN718.

The HIP temperature of 1160 °C was selected because HIP densification of PBF-LB IN718 saturates above 1150 °C at 100 MPa [23] and the Laves phase has been reported to dissolve completely at 1120–1150

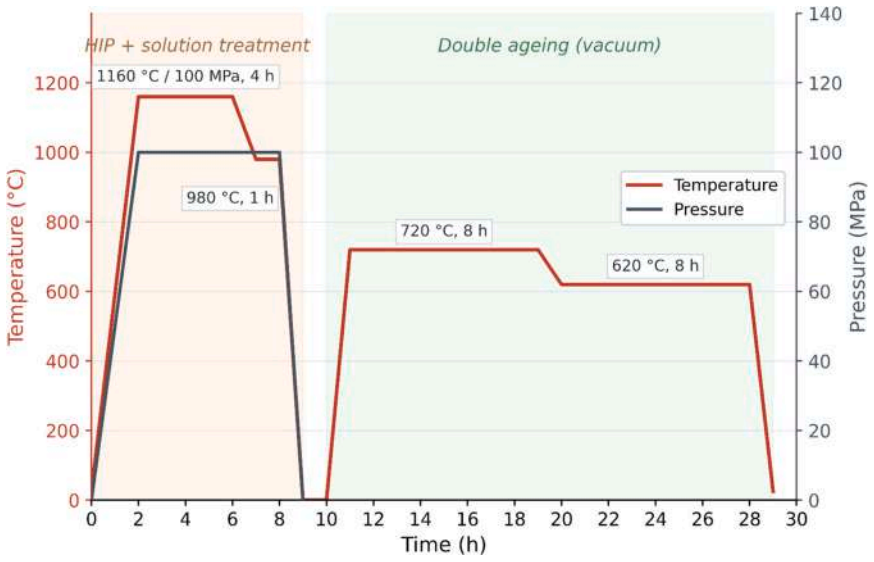

Fig. 1. Schematic representation of the HIP + heat-treatment applied to PBF-LB IN718.

°C [13,14]. In addition, complete recrystallisation within a hold time of a few hours requires at least 1150 °C, whereas higher temperatures promote grain growth: raising the HIP temperature from 1150 to 1180 °C increased the grain size after HIP + HT from 85.3 to 146.9 μm and reduced the yield strength from 1155 to 1005 MPa [13]. A temperature of 1160 °C therefore balances homogenization against grain coarsening.

2.3. Defect analysis

Porosity measurements were conducted in both as-built and post-HIPped conditions to quantify the HIP process's densification capability. Metallographic analysis was performed on phenolic resin-embedded specimens prepared using standard metallographic methods. This process included sectioning parallel (XZ) to the build direction of the samples so that the building direction can be observed for the complete layer analysis of the samples. All micrographs for porosity quantification were acquired from the core region of each section, excluding the edges and near-surface regions, to avoid contour-related and edge defects. Afterwards, grinding and polishing with SiC papers and polishing cloths ranging from 100 to 2400 grit, as well as diamond pastes containing particles from 6 to 0.1 μm, respectively. Optical micrography on the as-polished samples was performed using a metallographic microscope, Leica MEF4, at 50x.

Quantitative defect analysis was performed using ImageJ, an image analysis software, to determine the area fraction of porosity and pore size distribution. Defects were classified based on morphology and size to evaluate differences in HIP closure behavior.

The effectiveness of HIP densification was evaluated by comparing the initial porosity (P_0) with the residual porosity after HIP (P_{HIP}). A closure efficiency (η_{HIP}) parameter was calculated for each sample to assess the fraction of porosity eliminated during HIP processing as per the following equation:

$$\eta_{HIP}(\%) = \frac{P_o - P_{HIP}}{P_o} \times 100 \quad (3)$$

2.4. Microstructural characterization

After defect analysis of as-built and post-HIPped samples, microstructural characterization was also carried out to study the effect of PBF-LB parameters and HIP treatment conditions on the microstructure of the samples using optical microscopy and scanning electron microscopy in both secondary electron (SE) and backscattered electron (BSE) modes. Etched samples with Kalling 2 solution (5 g $CuCl_2$, 100 ml HCl, and 100 ml CH_3CH_2OH) etchant were examined for grain boundaries to reveal melt pool structures in the as-built condition and grain morphology after HIP treatment using a metallographic microscope, Leica MEF4. For grain size measurements, five intercepts were drawn on five different pictures for grain coarsening evaluation, and measurements were averaged as proposed in ASTM E112. However, clearer evolution of grain coarsening with VED of the PBF-LB was analyzed using Electron backscatter diffraction (EBSD).

While electronic microscopy was performed with a Scanning Electron Microscope EVO 15 (SEM) with an Energy-dispersive spectroscopy (EDS) probe by Oxford Instruments Ultim max 40 (40–170 mm2 sensor area) for analyzing precipitates, carbides, present in the microstructure. EDS was employed to identify Nb-rich regions and carbides and phase evolution associated with post-HIPped microstructure. Samples were observed at 5 and 100 KX, both in secondary and backscattered modes, depending on the particles to resolve, after chemical etching. Moreover, EBSD was employed to characterize the microstructure further, enabling detailed analysis of grain size distribution, grain boundary character (low-angle and high-angle grain boundaries), crystallographic texture, and grain orientation using a Tescan S9000G focused ion beam scanning electron microscope (FIB-SEM) equipped with an Oxford symmetry EBSD detector.

The recrystallized (RX) area fraction, derived from the GOS distribution using a 1° threshold, was adopted as a standard crystallographic proxy for recrystallization. However, a low GOS value can also result from recovery or from strain-free grains formed in situ during solidification, rather than from true recrystallization. For this reason, the HAGB fraction, which requires the actual formation of new high-angle grain boundaries, was used as a complementary, more conservative indicator, allowing the two mechanisms to be distinguished.

2.5. Hardness assessment

Nanoindentation tests were performed using a Hysitron model TI 950 TriboIndenter on both pre-HIPped and post-HIPped samples to evaluate the local mechanical response at the nanoscale. The tests were carried out using a standard loading profile of 15–15–15 s (loading–holding–unloading) with a maximum load of 1 mN. This technique enabled the determination of nano-hardness and elastic modulus at the nanoscale. A 6 × 6 indentation grid was performed on the samples with a 10-um distance between the indents. These were then translated into heatmaps using MATLAB, employing interpolation techniques to

represent the spatial distribution of hardness and modulus. Providing further insight into phase-specific mechanical behavior and microstructural heterogeneity.

3. Results and discussion

3.1. Evolution of defects with HIP

The optical micrographs of different PBF-LB IN718 samples in the as-built condition are shown in Fig. 2, representing the defect population with different printing parameters. The micrographs reveal multiple types of defects: spherical gas pores, pinholes, and irregular LOF defects. The spherical pores are typically associated with entrapped gas from the powder atomization process, shielding gas or instability in the melt pool, whereas the irregular and elongated defects originate from insufficient melting, inadequate overlap between scan tracks, or unstable melt pool dynamics. These LOF defects often appear along interlayer boundaries perpendicular to the building direction, reflecting the layer-by-layer nature of PBF-LB fabrication. Quantitative image analysis gave initial porosity values ranging from 0.01% in the well-optimized specimens to 17.76% in the severely under-melted ones, as tabulated in the supplementary material. This wide range enables direct evaluation of how the initial defect population influences the efficiency of HIP densification.

As shown in Fig. 3, initial porosity decreases with increasing VED, but the relationship is not single-valued: at a given VED the measured porosity spans up to two orders of magnitude, and this spread is systematic rather than random. Considering the overall trend first, for VED below ~60 J/mm^3 , porosity rises steeply, consistent with the transition from stable conduction-mode melting to an unstable regime dominated by discontinuous melt tracks and lack-of-fusion voids. This threshold is in good agreement with values reported for PBF-LB processing of nickel-based superalloys, where complete powder melting and adequate track overlap typically require VED above 50–60 J/mm^3 , depending on powder characteristics and machine parameters [29,30]. Above approximately 80 J/mm^3 , porosity falls below 5%, and the trend flattens, indicating that further increases in energy input yield diminishing returns in densification while progressively increasing the risk of keyhole-induced porosity above ~170 J/mm^3 .

The dominant feature of Fig. 3 is the complete separation of the 100 W population from the 150 W and 200 W populations. All ten specimens built at 100 W lie above the 0.5% porosity line, while all twenty specimens built at 150 W or 200 W lie below it, and the two groups do not overlap anywhere in the build matrix: the least porous 100 W specimen (0.71%, sample 4, 79 J/mm^3) remains more porous than the most porous 150 W specimen (0.42%, sample 18, 56 J/mm^3), even though the latter was processed at a 30% lower VED. At same VED, the difference reaches one to two orders of magnitude: 2.31% at 111 J/mm^3 and 100 W against 0.02% at 119 J/mm^3 and 150 W, and 13.06% at 67 J/mm^3 and 100 W against 0.18% at 69 J/mm^3 and 150 W.

This behavior follows directly from the fact that VED is a lumped descriptor rather than a state variable. Melt pool penetration scales with the normalized enthalpy, $\Delta H/h_s \propto P/\sqrt{v}$ for a fixed beam diameter, whereas VED $\propto P/(v{\cdot}h{\cdot}t)$; hatch spacing and layer thickness enter the energy equation but not the penetration depth of an individual track. Traversing a line of constant VED from 100 W to 200 W therefore increases $\Delta H/h_s$ by a factor of $\sqrt{2}$ even though the nominal energy input is unchanged. Consistently, porosity within the 100 W set is governed almost entirely by scan speed rather than by VED: samples 3 and 7 were built at nominally the same energy density (67 and 62 J/mm^3) yet differ by a factor of sixteen in porosity (13.06% against 0.80%), the only substantive difference being the scan speed (1500 against 900 mm/s), with the more closely spaced hatch producing the higher porosity.

The morphology and gas content of these defects largely determine their response to HIP. In the present specimens, the two populations are clearly distinguishable: samples processed below ~60 J/mm^3 contain

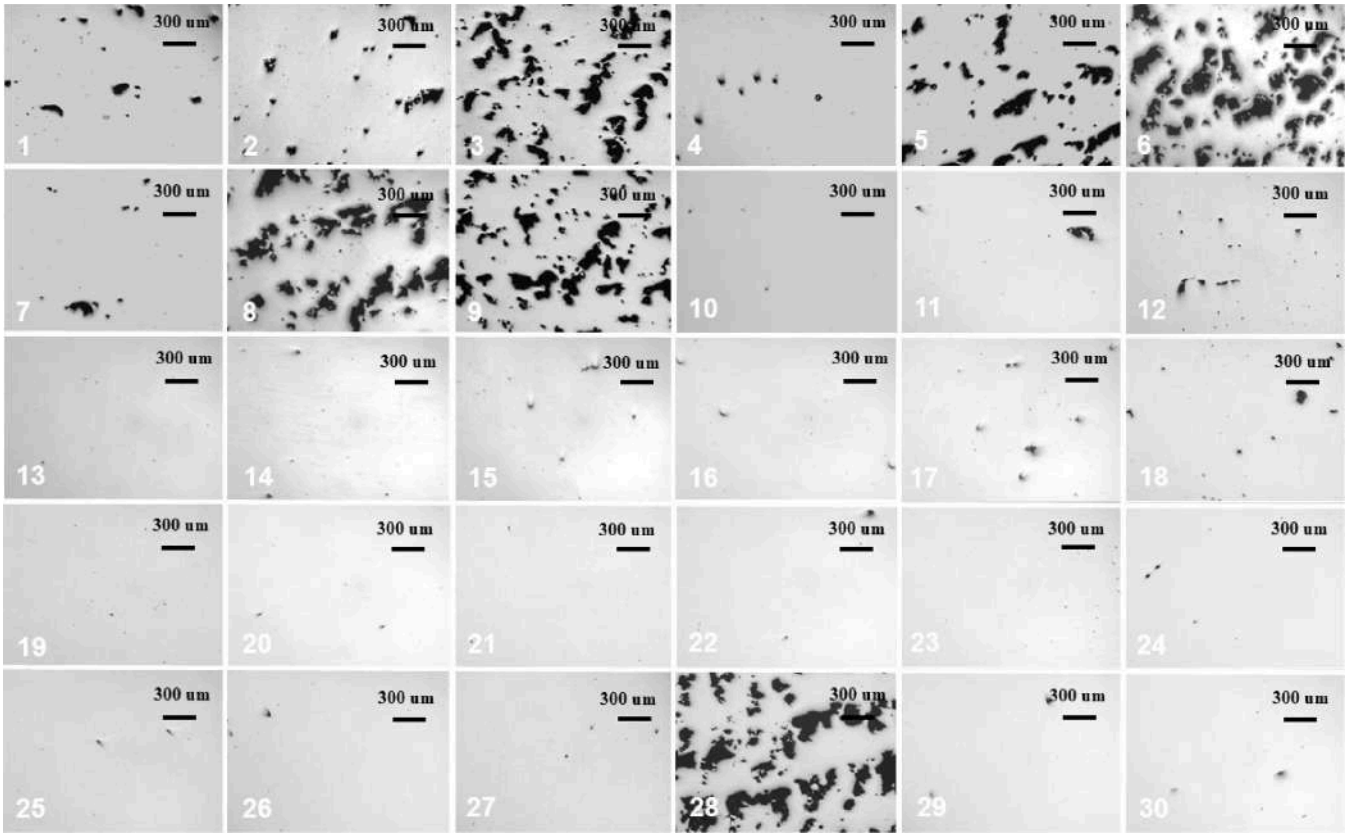

Fig. 2. Optical micrographs showing the pore distribution in as-built PBF-LB IN718 before HIP.

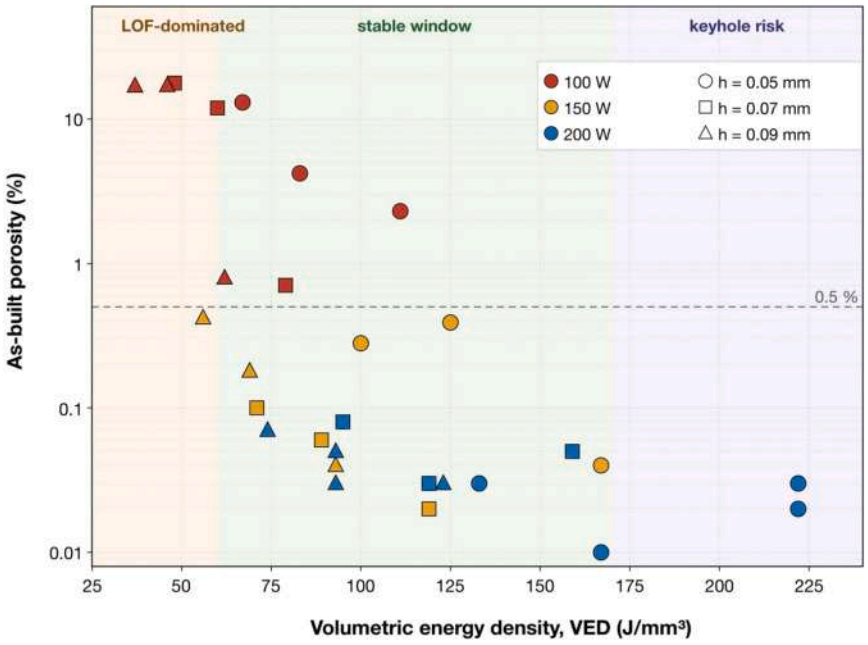

Fig. 3. Initial porosity (%) and energy density (J/mm^3) of IN718 samples arranged in decreasing order of initial porosity, showing an inverse relationship between the two parameters.

large, irregular lack-of-fusion defects with aspect ratios exceeding 3:1, whereas those processed above ~100 J/mm^3 contain predominantly spherical pores below 100 μm in diameter. Following the closure criterion introduced in Section 1, these two populations are expected to behave very differently. The irregular defects present large radii of curvature and unbonded rather than gas-filled interfaces, and are therefore expected to collapse readily under the applied pressure, provided they remain enclosed. The spherical pores, by contrast, are argon-filled and fine, so both terms opposing closure act simultaneously, and they represent the population least likely to be eliminated. This distinction is examined quantitatively in Section 3.1.1 through the pore size distributions before and after HIP.

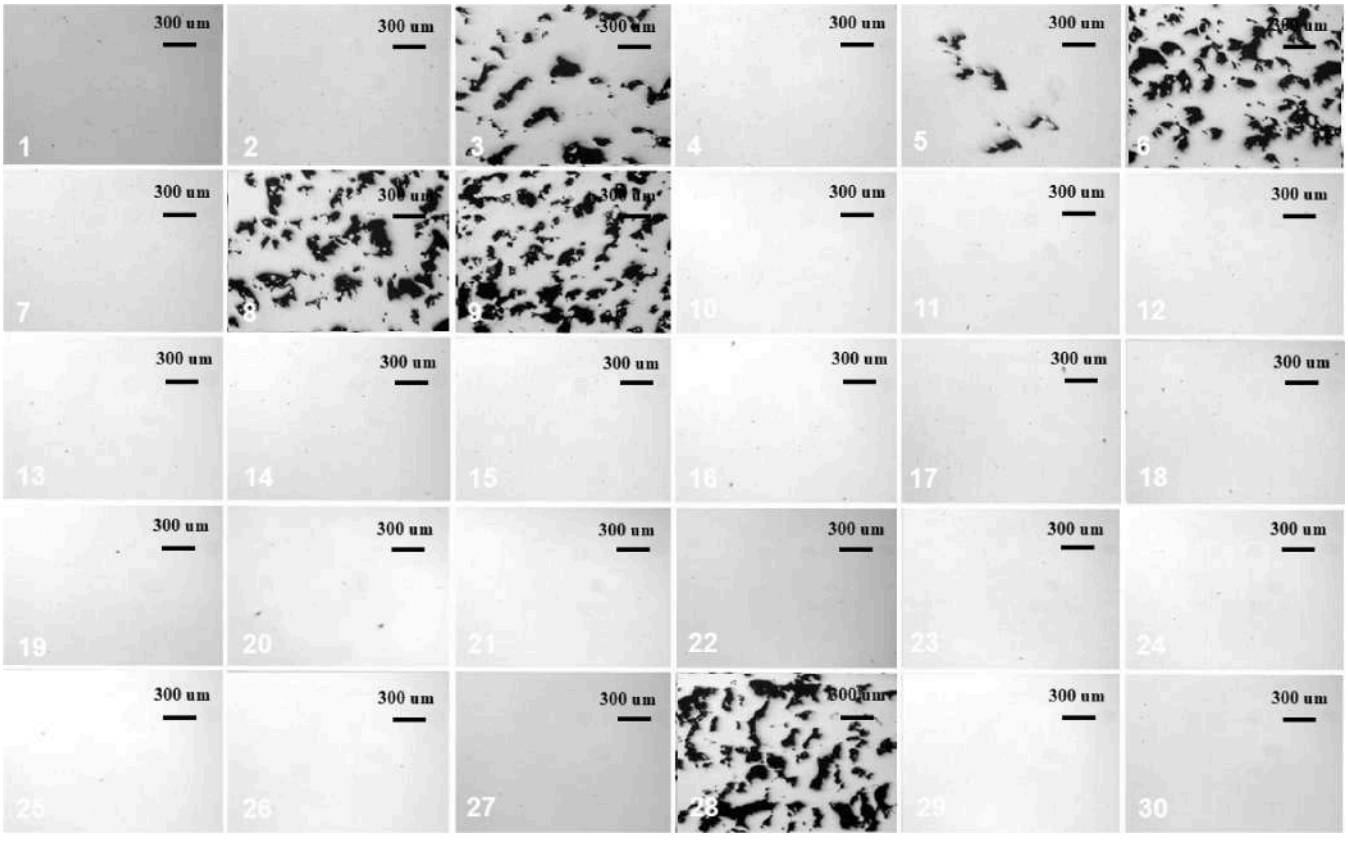

Fig. 4. Optical micrographs showing the pore distribution in as-built PBF-LB IN718 after HIPping.

After HIP treatment, a clear reduction in porosity is observed in the majority of the samples, as seen in Fig. 4. Samples with low initial porosity show almost complete densification, with porosity approaching negligible levels. Samples with moderate initial porosity, most of the isolated defects are either eliminated or reduced to extremely small sizes, as it had both closed and open pores. And then samples with initial porosity $\geq$ 17% show an increase in porosity after HIPping. Based on the above observations in post-HIPped samples, the samples are divided into three categories:

First, porosity levels are already low, mostly in the form of gas porosity. In these samples, trapped argon and post-HIP heat treatment in thermally induced porosity play an important role. Even for enclosed pores, gas-filled porosity can persist after HIP because inert gas has limited solubility in the metal lattice, making complete closure thermodynamically and kinetically challenging. However, once a pore has been closed by creep and diffusional bonding of its surfaces, it cannot reopen on depressurization alone, since the deformation is plastic and the pore surfaces are metallurgically bonded. Incompletely closed argon-filled pores, however, remain susceptible during subsequent high-temperature exposure. As the temperature increases, the pressure of the entrapped gas rises while the flow stress of the surrounding matrix decreases, so that in the absence of an external constraint the pore can cause porosity again by creep. This thermally induced porosity is typically reported for treatments carried out at temperatures at or above the HIP temperature, or at somewhat lower temperatures when the external pressure is low, as is the case for the vacuum ageing. Prior IN718 studies have linked high initial porosity and argon-filled pores to post-processing sensitivity, including differences between ageing under pressure versus at ambient conditions [22].

Second is the regime of moderate initial porosity, approximately 0.1–10%, which shows the sharpest decrease in defect content. These defects are typically associated with incomplete bonding or pinholes due to overheating, in addition to gas pores, allowing the surrounding material to collapse and weld together during the HIPping cycle. Pore-closure literature similarly reports that large irregular pores can close faster than small spherical pores [31].

However, as the porosity levels approaching 17%, HIPping shows no improvement in the third type of samples. As the percentage of defects increases, the defects convert from closed pores to open pores, making the internal and external HIP pressure difference zero. Classical HIP theory explains effective closure of enclosed pores through creep/plasticity and diffusion, but requires a pressure differential across the pore surface. If LOF defects form interconnected networks that connect to the environment, capsule-free HIP allows argon penetration, removing the driving pressure differential and preventing closure. This mechanism is consistent with AM and HIP studies documenting that open-to-surface defects are intrinsically difficult or impossible to eliminate without encapsulation [11].

As the initial porosity further increases, it leads to an increase in defect content after the HIP + heat treatment cycle. This behavior is particularly evident for samples 6, 8, 9, and 28, where the final porosity exceeded the initial values, depicted in Fig. 5. Examination of micrographs suggests that this phenomenon is associated with open porosity, where the external pressure is equal to the internal pressure, making the closure of the porosity impossible. Moreover, in certain cases where the gas is entrapped in the large pores and sealed inside may expand during the post-HIP heat treatment, increasing the defect size. Despite the general effectiveness of HIP, the results clearly demonstrate that densification efficiency strongly depends on the initial defect population.

From the above results, we can conclude that a key factor resulting in pore closure during HIPping is the balance between external pressure and internal gas pressure. Moreover, this situation becomes particularly significant during the ageing stage, which was performed under vacuum conditions. Under vacuum, the external pressure resisting pore expansion is minimal, allowing trapped gas to expand and reopen previously compressed defects at high temperature. Consequently, pores may grow or coalesce, as the defects look more interconnected in the samples where the defect percentage shows an increase, which explains the increase in defect area observed in some samples. This phenomenon is consistent with the observations reported by Kaletsch et al. [22] discussed in the introduction section, supporting the observations in the present work, indicating expansion of argon-filled pores and partial reopening of previously compressed defects as ageing was performed under vacuum.

Entrapped argon in PBF-LB IN718 has been confirmed by Tillmann et al. [23], who measured a higher argon content in PBF-LB built specimens than in conventionally manufactured material and attributed it to the argon build atmosphere and to gas-filled pores in the gas-atomised powder. In samples with open porosity, the pressurized argon of the HIP vessel may additionally infiltrate the interconnected defects and become sealed inside them, further contributing to pore expansion

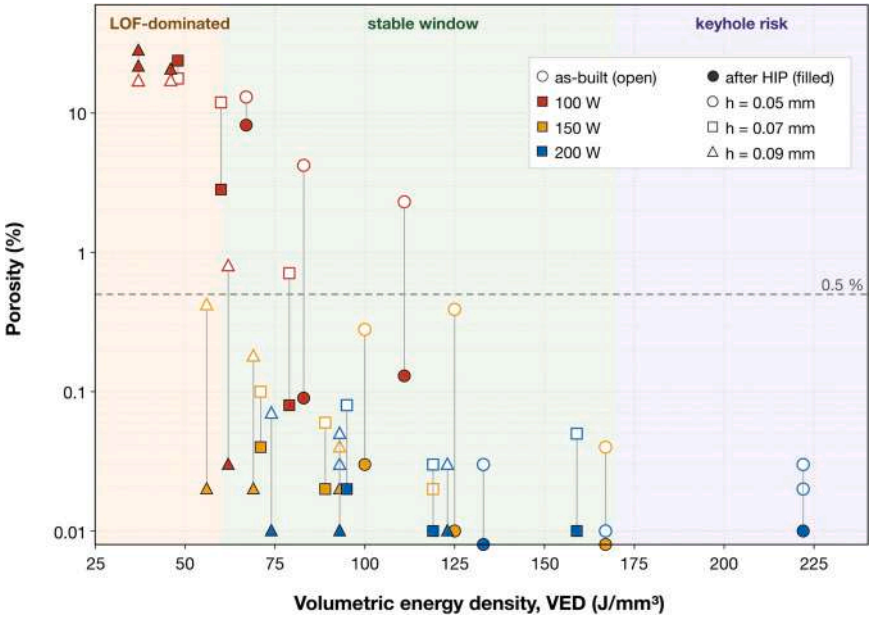

Fig. 5. Variation of Porosity Across PBF-LB IN718 Samples Before and After HIP Treatment.

during vacuum ageing.

3.1.1. Analysis of pore closure based on size

The pore size distribution, presented as pore count versus equivalent circular diameter (ECD) in Fig. 6, provides quantitative insight into the size-dependent nature of HIP densification. Pooled over all thirty specimens, the total population decreases from 8787 to 7467 pores, a net reduction of 15.0%, but this figure covers a strongly non-uniform response across the size classes. The smallest resolvable defect in the present analysis was 2.2 μm ECD, which defines the lower bound of the first class.

The finest class, spanning 2.2–30 μm, dominates the population in both conditions, comprising 6999 pores before HIP and 6265 after, a reduction of only 10.5%. These are predominantly spherical, gas-filled defects originating from argon entrapped during atomization or PBF-LB processing. Their persistence is consistent with the closure criterion introduced in Section 1: both terms opposing closure, the internal argon pressure and the surface-energy contribution $2\gamma/r$, act most strongly on the finest pores, so this class is the least amenable to elimination.

The 30–60 μm class shows the largest fractional reduction of the whole distribution, falling from 825 to 416 pores (−49.6%), and therefore represents the most HIP-responsive population. Above this class the response weakens and becomes size-independent rather than progressive: reductions of 30.3% (340−237) at 60–90 μm, 13.4% (216−187) at 90–120 μm, 23.8% (130−99) at 120–150 μm, 24.2% (120−91) at 180–240 μm and 20.5% (39−31) at 240–300 μm, with the 150–180 μm class essentially unchanged (102−105). The single exception to the overall reduction is the class exceeding 300 μm, which increases from 16 to 36 pores, a rise of 125%. Two processes contribute: coalescence of adjacent lack-of-fusion defects into larger interconnected voids, and growth of large argon-filled defects, as described in Section 3.1.

3.2. Microstructural evolution before and after HIP + heat treatment

3.2.1. Optical microstructure before and after HIP

Fig. 7 compares the etched optical micrographs of samples 28, 29 and 30, processed at 37, 93 and 222 J/mm^3 , respectively, in the as-built and post-HIP conditions. These three conditions span the processing window and correspond to the specimens examined by EBSD in Section 3.2.3. The two rows are shown at different magnifications, since melt pool boundaries and recrystallized grains differ in scale by roughly an order of magnitude; scale bars are given in each panel. Micrographs for the complete set of thirty specimens are provided as supplementary material.

In the as-built condition, the microstructure is dominated by melt pool boundaries, visible along the build direction as overlapping semi-circular arcs that reflect the localized melting and rapid solidification of successive powder layers. Individual grain boundaries are not resolved at this magnification, and the as-built grain morphology is instead characterized by EBSD. At 37 J/mm^3 the melt pools are shallow and poorly overlapped, with large irregular lack-of-fusion voids interrupting the layer sequence, whereas at 93 and 222 J/mm^3 , the arcs are continuous and the structure is essentially defect-free.

Melt pool dimensions measured across the full matrix are reported in Fig. 8. The depth-to-width ratios lie between approximately 0.15 and 0.28, consistent with stable conduction-mode processing [32,33], but neither depth nor width correlates significantly with VED ($r = -0.34$, $p = 0.068$ and $r = +0.26$, $p = 0.17$ respectively). The controlling variable is instead laser power, as the separation by symbol colour in Fig. 8 (b) makes clear: mean width increases from 112 μm at 100 W to 128 μm at 150 W and 143 μm at 200 W, with little systematic variation along the VED axis within each power level, while mean depth remains invariant at 26.8, 25.5 and 26.5 μm. Melt pool geometry is therefore governed by the individual process parameters rather than by their lumped combination, consistent with the defect results of Section 3.1: hatch spacing

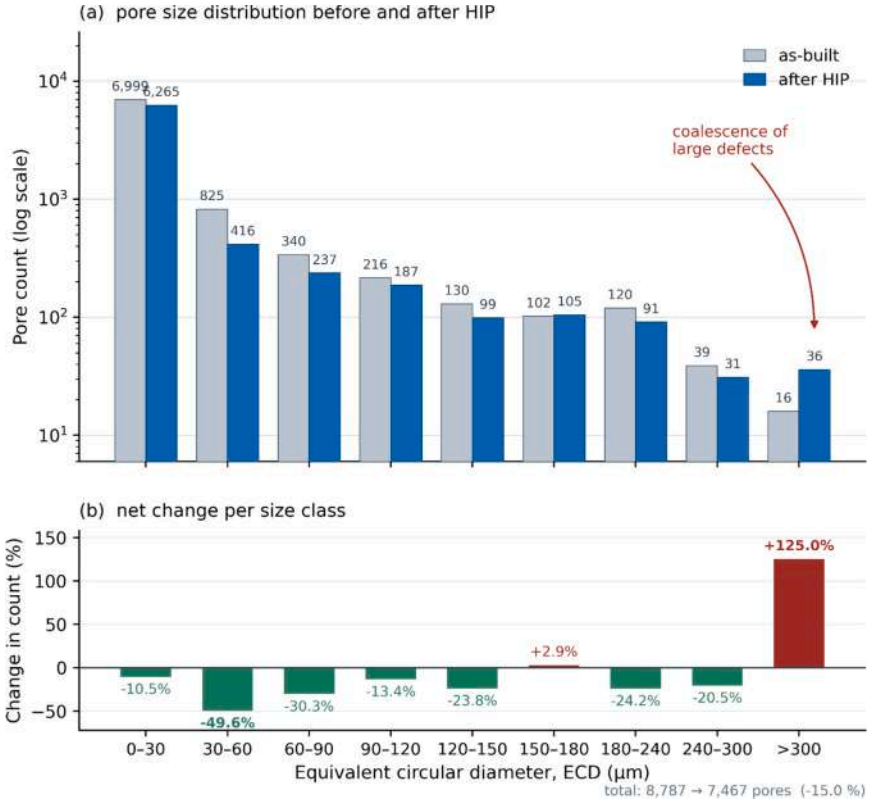

Fig. 6. Pore size distribution of PBF-LB IN718 in terms of pore count versus equivalent circular diameter (ECD), (a) as-built and post-HIP counts per size class on a logarithmic scale; (b) net change in count per class.

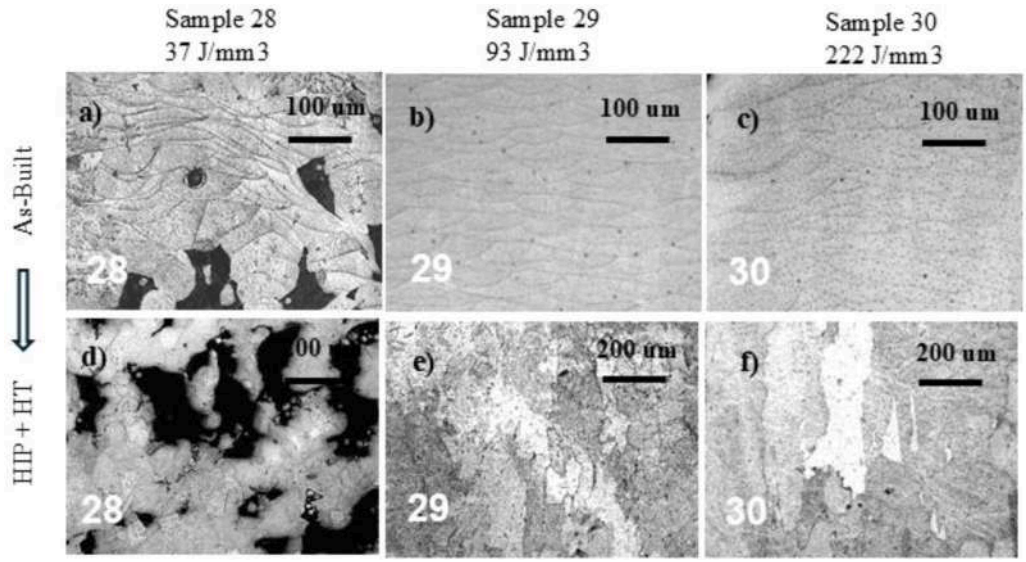

Fig. 7. Etched micrographs of PBF-LB IN718 samples in the as-built condition showing melt pool morphology.

and layer thickness enter the energy calculation but not the geometry of an individual track. The narrower melt pools measured at 100 W account for the reduced track overlap and the persistent porosity of that group.

After HIP and heat treatment, the melt pool boundaries are absent in these three specimens and across all thirty, irrespective of initial porosity (provided as supplementary material), confirming that the cycle homogenizes the solidification structure independently of the defect population. Their disappearance reflects dissolution of the interdendritic segregation network that produced the etching contrast, examined in Section 3.2.2. The transition from columnar to equiaxed morphology is quantified in Section 3.2.3.

Residual porosity remains clearly visible in sample 28, where the interconnected lack-of-fusion voids persist and are more extensive than in the as-built condition, consistent with the negative closure efficiency reported in Section 3.4. Samples 29 and 30 show no resolvable porosity. The optical evidence therefore separates the two effects of the HIP cycle: homogenisation is achieved uniformly across the processing window, whereas densification is strongly conditional on the initial defect state.

To further analyze the as-built microstructure in more depth, SEM images were analyzed, which reveal a fine cellular-dendritic substructure aligned along the thermal gradient. The rapid cooling rates inherent to PBF-LB processing, typically on the order of 10^5–10^6 K/s, result in extremely fine microstructural features compared with conventional processing routes with highly segregated areas. Specifically, these Nb-enriched regions are often associated with the formation of laves phases [$(Ni,Fe,Cr)_2Nb$], as described in the literature [22,34], which are known to degrade mechanical properties by reducing the amount of Nb available for strengthening precipitates [35].

3.2.2. SEM microstructure before and after HIP

Higher-resolution examination by SEM, presented in Fig. 9, resolves the sub-grain features underlying the optical observations. In the as-built condition, the material exhibits a fine cellular–dendritic substructure formed during rapid solidification, with cell boundaries appearing bright owing to enrichment in niobium rejected from the solidifying γ. The morphology of this substructure varies between locations within a single specimen, as shown in Fig. 9(b) and (c). Discrete particles consistent with the Laves phase [$(Ni,Fe,Cr)_2Nb$] are present along these boundaries, in agreement with previous reports for PBF-LB IN718 [22,23].

After HIP and heat treatment, the cellular network and its associated contrast are no longer detectable, and no Laves particles were observed, indicating that the 1160 °C hold is sufficient to dissolve this phase and return Nb to solid solution in the γ matrix. Two secondary phases are instead present, both located at grain boundaries: needle-like precipitates identified as δ-phase (Ni_3Nb) and blocky particles identified as MC carbides, the latter confirmed as Nb- and C-rich by the EDS spectra in Fig. 9(f). The δ-phase distribution is moderate and predominantly intergranular. At higher magnification, Fig. 9(e), a fine and spatially uniform distribution of nanoscale precipitates is resolved within the grain interiors, corresponding to the γ′ and γ″ phases formed during double ageing.

In the as-built state, Nb is concentrated in a continuous network at the solidification cell boundaries, where it is locked into the brittle Laves phase and unavailable for strengthening. After HIP and ageing, the same Nb is distributed as a fine, uniform population of γ″ precipitates inside the grains, with only isolated δ-phase needles and MC carbides left at the boundaries. This sequence of Laves dissolution followed by γ′/γ″ reprecipitation is well established for heat-treated PBF-LB IN718 and is the reason the alloy recovers its strengthening response after post-processing. It also explains the reduction in local property scatter reported in Section 3.3, since the hard interdendritic regions and softer cell interiors of the as-built condition are replaced by a uniformly precipitation-hardened matrix.

3.2.3. EBSD analysis and crystallographic texture evolution

EBSD analysis was performed on three representative samples, namely 28, 29, and 30, fabricated at VED values of 37, 93, and 222 J/mm^3 , respectively, thus spanning the processing window from its lower to its upper limit. For each sample and condition, Fig. 10 presents the EBSD inverse pole figure (IPF) coloring maps from the transverse section and the corresponding pole figures.

In both conditions, sample 28 shows a fragmented, pore-rich microstructure resulting from the sub-optimal printing conditions. Although the IPF maps do not reveal a clear orientation distribution, the pole figures show significant differences between the as-built and HIPped states. In particular, the as-built sample presents the typical fiber texture in the {100} pole figure, with a preferential grain orientation along the building direction. After the HIP treatment, by contrast, all three pole figures display an almost random intensity distribution. Unlike sample 28, the IPF maps of samples 29 and 30 in the as-built state present a very evident preferential grain orientation, which is further confirmed by the pole figures. Indeed, both samples exhibit a clearly defined fiber texture, with a strong orientation along the building direction in the {100} pole figure and the typical rings modulated by four

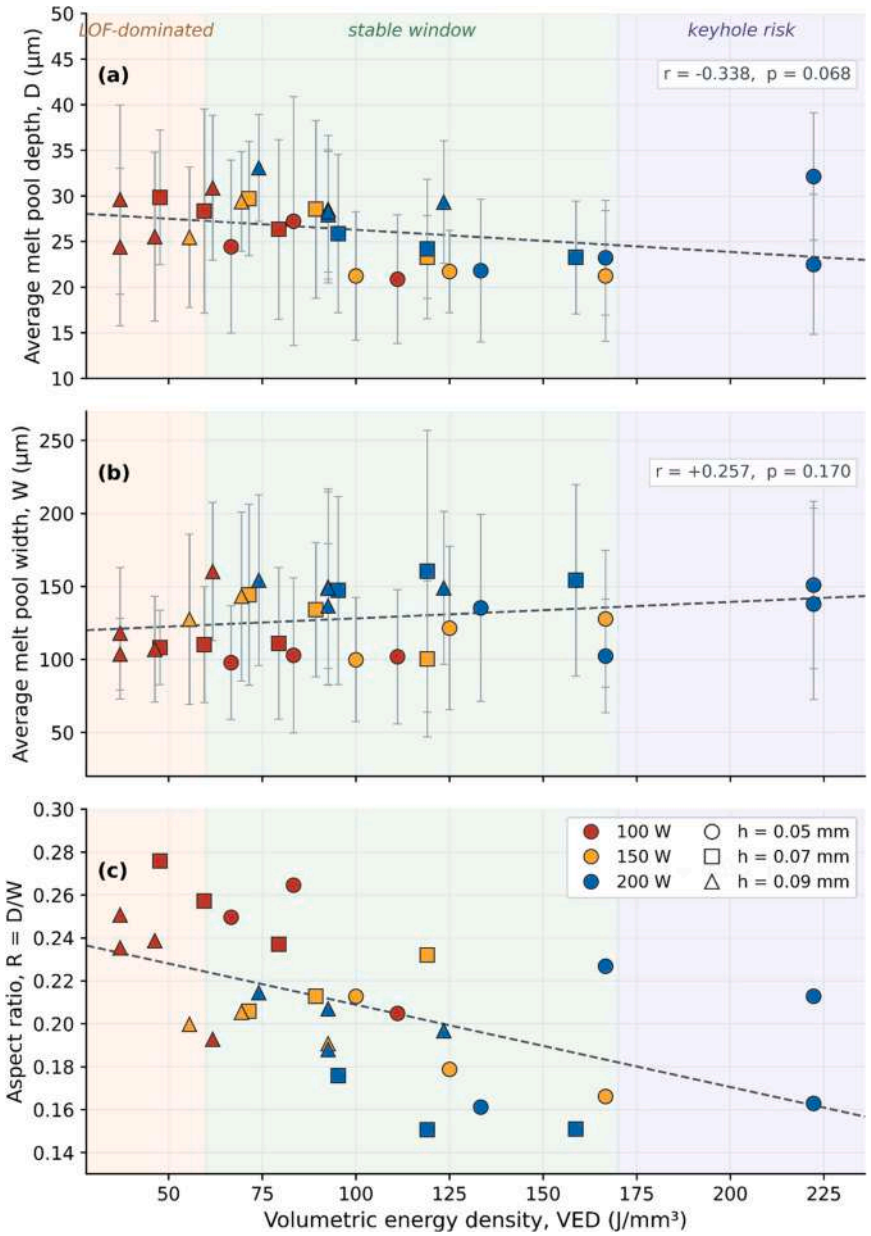

Fig. 8. Variation of melt pool geometry in PBF-LB IN718 samples showing (a) average melt pool height, (b) average melt pool width, (c) aspect ratio (R = D/W).

intensity maxima in the {110} and {111} pole figures. As observed for sample 28, both samples become randomly oriented in the HIPped state [36].

To evaluate recrystallization also in quantitative terms, several EBSD-derived quantities were considered (Table 2). It was assessed both from a crystallographic standpoint, using parameters such as the High-Angle Grain Boundary (HAGB) fraction, the recrystallized (RX) area fraction and the average Grain Orientation Spread (GOS), and from a morphological standpoint, using the Fitted Ellipse Major Diameter (FEMD) and the Aspect Ratio (AR). The RX area fraction was derived from the GOS values, taking 1° as the threshold below which a grain was considered recrystallized.

From a crystallographic perspective, sample 29 clearly shows the most extensive and nearly complete recrystallization, reaching the highest post-HIP values of HAGB fraction and RX area fraction together with the lowest average GOS, all three being strong indicators of the recrystallized state. It attains this level even though its as-built condition closely resembles that of sample 30, which records lower post-HIP values. Sample 28 instead ends up with the lowest HAGB fraction, while its RX area fraction remains comparable to that of sample 29, although it starts from a higher as-built value. Its as-built state is the least deformed of the three, consistent with a lower stored energy and therefore a weaker driving force for recrystallization.

This behavior can be traced back to the underlying melt pool dynamics. As demonstrated by Son et al., increasing laser power and hence VED enlarge the melt pool, accelerating conductive heat dissipation into the substrate. The resulting higher cooling rates produce greater thermal stress and a higher dislocation density in the as-built state, which raises the stored energy available as driving force for recrystallization during HIP [37]. At low VED, moreover, strain-free grains already present in the as-built state may originate from in situ recrystallization driven by the intrinsic thermal cycling of the process, yet they lack the dislocation density required to drive a complete microstructural transformation during subsequent heat treatment [38]. This is the case of sample 28, whose as-built RX area fraction is the highest of the three. Its high post-HIP value therefore reflects the recovery of a structure that was partly strain-free from the start. In this case the HAGB fraction, which requires the formation of new high-angle boundaries, remains the more

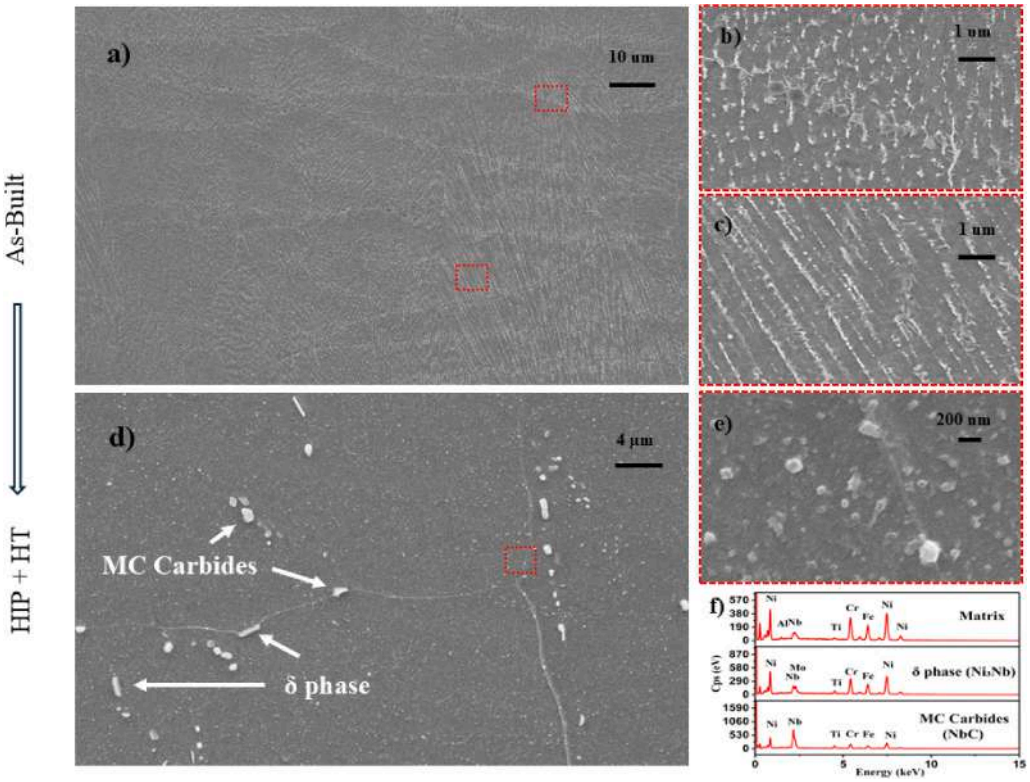

Fig. 9. SEM micrographs of PBF-LB IN718 (a–c) in the as-built condition, showing the cellular–dendritic substructure with Nb-rich interdendritic boundaries, and (d, e) after HIP and double ageing, showing MC carbides and δ-phase at the grain boundaries and fine γ′/γ″ precipitates within the matrix; (f) EDS spectra of the matrix, δ-phase and MC carbides.

discriminating parameter. The fitted GOS distributions (Fig. 11) show that HIP does not merely shift the average but collapses the population into a narrow low-misorientation peak. The contraction is steepest in sample 29, where only 1% of grains are located above the 1° threshold used to identify recrystallized grains. Sample 30 has a peak close to that of sample 29 but retains by far the broadest post-HIP distribution, with 14% of grains still exceeding 1°. This residual tail, rather than a uniformly higher misorientation, accounts for its lower RX area fraction, and is consistent with the highly strained grain clusters not yet consumed by the growth of new recrystallized grains reported by Deirmina et al. [38] Sample 28 exhibits the most uniform distribution in the as-built state; however, it narrows to a lesser extent than the other samples after HIP, and consequently its peak sits at the highest GOS value among the HIPped conditions.

Morphologically, sample 28 exhibits the lowest aspect ratio, corresponding to more equiaxed grains, followed by sample 29, which undergoes the largest reduction from the as-built to the HIPped state, and then sample 30. The average FEMD shows no reduction for sample 28, increasing slightly from 41.2 to 45.0 µm, whereas the other two samples display an average size reduction owing to the formation of new fine grains during recrystallization. The fitted AR distributions (Fig. 12) clarify the origin of this morphology. In the as-built state samples 29 and 30 are dominated by an elongated population, as reflected by the extended tail, while sample 28 has a markedly narrower distribution. The low aspect ratio of this last sample should not be taken as an indication of extensive recrystallization, since it reflects the more equiaxed grain structure typical of low VED processing, where smaller volume of previously solidified material is remelted upon deposition of the new layer. After HIP all three converge towards a mode of about 1.4–1.5, although sample 30 preserves the longest tail.

3.2.4. *Coupling between energy density, defect population and recrystallisation response*

The defect and EBSD results are not two independent outcomes of the process: both are set by the same melt pool, and this coupling offers a qualitative interpretive framework for why the recrystallisation response is non-monotonic with volumetric energy density. This framework is not independently quantified and is summarized only schematically in Fig. 13.

At low VED (37 J/mm^3, sample 28) the melt pools are small and poorly overlapped, so a large fraction of the deposited volume is never remelted. Two consequences follow simultaneously. First, the material contains extensive interconnected lack-of-fusion porosity (P_o = 17.76%), which removes the pressure differential required for HIP closure and leaves the specimen with a higher final porosity than the as-built state. Second, the solidified volume is only weakly constrained by its surroundings and experiences a limited number of thermal cycles, so the as-built structure stores comparatively little deformation energy: the average GOS is 1.6°, the lowest of the three conditions, and 14.1% of the area is already strain-free, consistent with in-situ recrystallisation driven by the intrinsic thermal cycling of the process rather than with a genuinely recovered deformed structure. During HIP, this material therefore recovers rather than recrystallizes: the RX area fraction reaches 96.8%, but the HAGB fraction stops at 82.3%, the lowest of the three, and the average grain size does not decrease (from 41.2 to 45.0 µm) because few new high-angle boundaries are generated. In this regime, the HAGB fraction, which requires the actual formation of new boundaries, is the more discriminating indicator of recrystallisation than the GOS-derived RX fraction.

At intermediate VED (93 J/mm^3, sample 29) the scan tracks overlap continuously and the material is essentially fully dense (P_o = 0.05%). The columnar solidification structure that develops (AR = 5.3, FEMD = 107 µm) is strongly deformed, with an average GOS of 2.4°, and the absence of defects means that boundary migration is not obstructed by

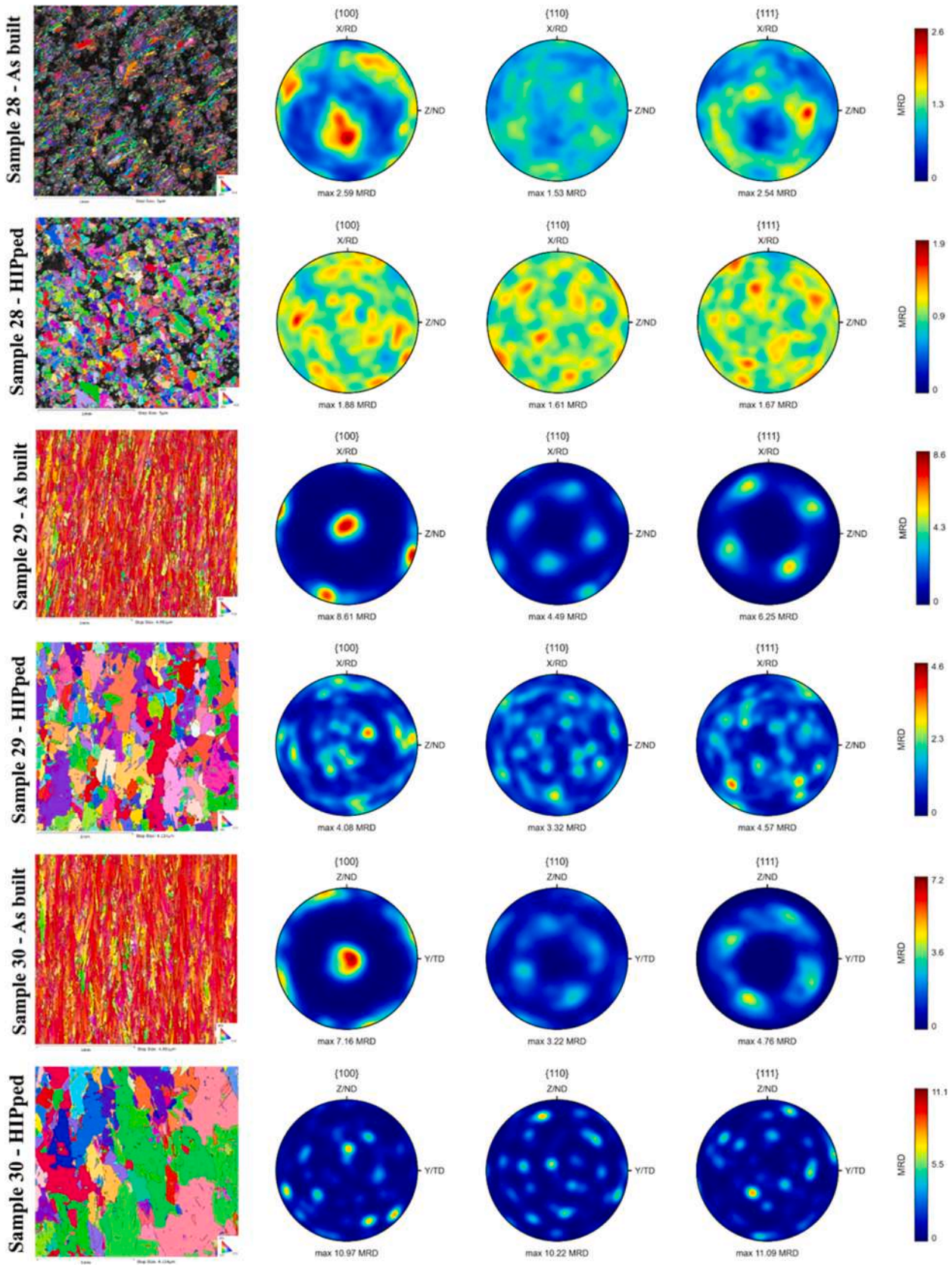

Fig. 10. IPF maps with the corresponding pole figures of as-built and HIP conditions for samples 28, 29 and 30.

Table 2
EBSD summary of HAGB, GOS, RX area, AR and FEMD.

Sample	VED (J/mm^3)	Condition	HAGB (%)	Avg GOS (°)	RX area (%)	Avg AR	Avg FEMD (μm)
28	37	AB	47.6	1.6	14.1	2.7	41.2
		HIP	82.3	0.6	96.8	1.9	45.0
29	93	AB	58.7	2.4	3.0	5.3	107.4
		HIP	99.2	0.3	97.5	2.4	80.3
30	222	AB	60.6	2.5	3.3	4.4	119.7
		HIP	93.1	0.6	92.4	3.1	90.8

pores or unbonded interfaces. This combination of a high driving force and an uninterrupted matrix produces the most complete transformation of the whole set: HAGB rises to 99.2%, the RX area fraction to 97.5%, only 1% of the grains remain above the 1° GOS threshold, and the grain size is genuinely refined (from 107.4 to 80.3 μm) by the nucleation and growth of new grains.

Increasing VED further to 222 J/mm^3 (sample 30) does not improve the response, and in fact degrades it. The as-built stored energy has already saturated (GOS 2.5°, essentially the same as sample 29), so no additional driving force is gained, while two penalties appear. The wider melt pools and the associated heat accumulation coarsen the as-built columnar structure (FEMD = 119.7 μm), reducing the density of grain boundaries that act as preferential nucleation sites for recrystallisation and increasing the distance that a recrystallisation front must sweep to consume the deformed matrix. In parallel, the onset of keyhole instability reintroduces spherical, argon-filled porosity. The result is an incomplete transformation: HAGB stops at 93.1%, the RX area fraction at 92.4%, and 14% of the grains still exceed the 1° threshold after HIP. Importantly, the post-HIP GOS distribution of this sample peaks close to that of sample 29 but retains a much broader tail, which indicates that the residual deformation is not uniformly distributed but concentrated in strained grain clusters that have not yet been consumed by the growth of new recrystallised grains. The final structure is consequently the coarsest (90.8 μm) and the least equiaxed (AR = 3.1) of the three.

The recrystallisation response after HIP can *qualitatively* be rationalised as reflecting two competing, VED-governed tendencies inferred from the measured EBSD and defect trends not from an independently measured or fitted quantity: the stored energy available as driving force, which is expected to increase with VED and saturate above ~100 J/mm^3 based on the plateau in as-built GOS between samples 29 and 30, and the density of potential nucleation sites, which is expected to decrease as the as-built grains coarsen based on the measured increase in FEMD. Neither term, nor their product, is quantified independently of the recrystallisation outcome itself; the maximum in the intermediate VED range is therefore an interpretive pattern drawn from the three measured conditions rather than a demonstrated functional relationship, and it coincides with the range where the initial porosity is already low enough for HIP to be effective but not yet high enough for keyhole defects to appear. This convergence is the practical message of the present work: the same process window that minimises the pre-HIP defect population also maximises the microstructural benefit obtained from the HIP cycle, so densification and microstructural homogenisation should be qualified together rather than as separate post-processing objectives.

It is worth noting that the grain coarsening observed at high VED, while measurable, does not undermine the primary objectives of the selected HIP cycle. The HIP temperature of 1160 °C was chosen specifically to maximize pore closure efficiency and to ensure complete dissolution of Nb-rich Laves phases, thereby enabling the subsequent precipitation of a uniform distribution of γ'/γ'' strengthening phases during double ageing. Although higher HIP temperatures are known to promote grain growth, and hence a strength–ductility trade-off, in IN718 and related nickel superalloys, this consideration is of secondary

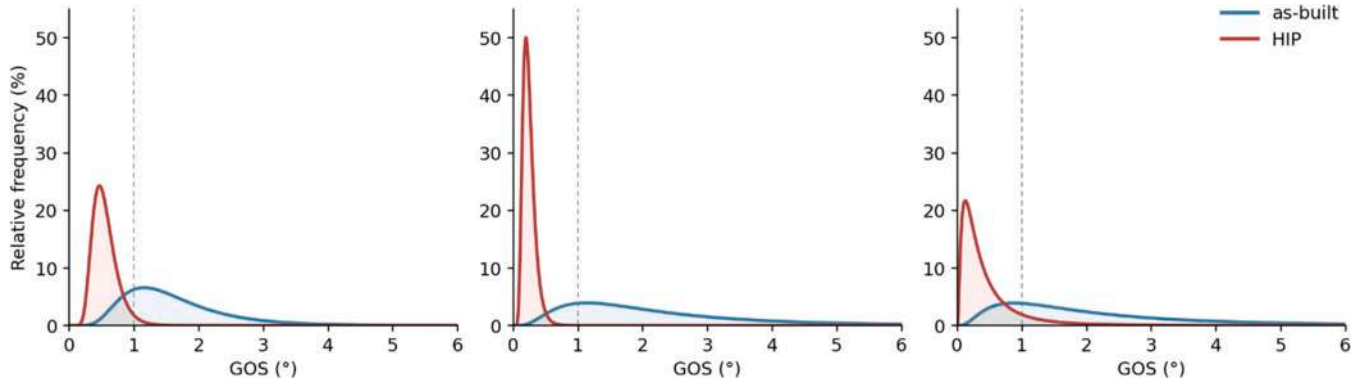

Fig. 11. Fitted GOS distributions of as-built and HIP conditions for samples 28, 29 and 30.

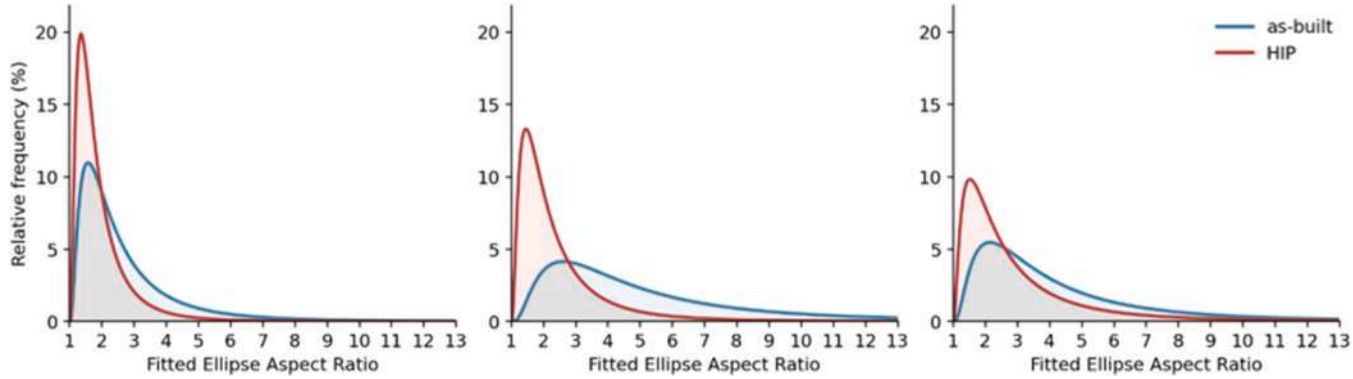

Fig. 12. Fitted AR distributions of as-built and HIP conditions for samples 28, 29 and 30.

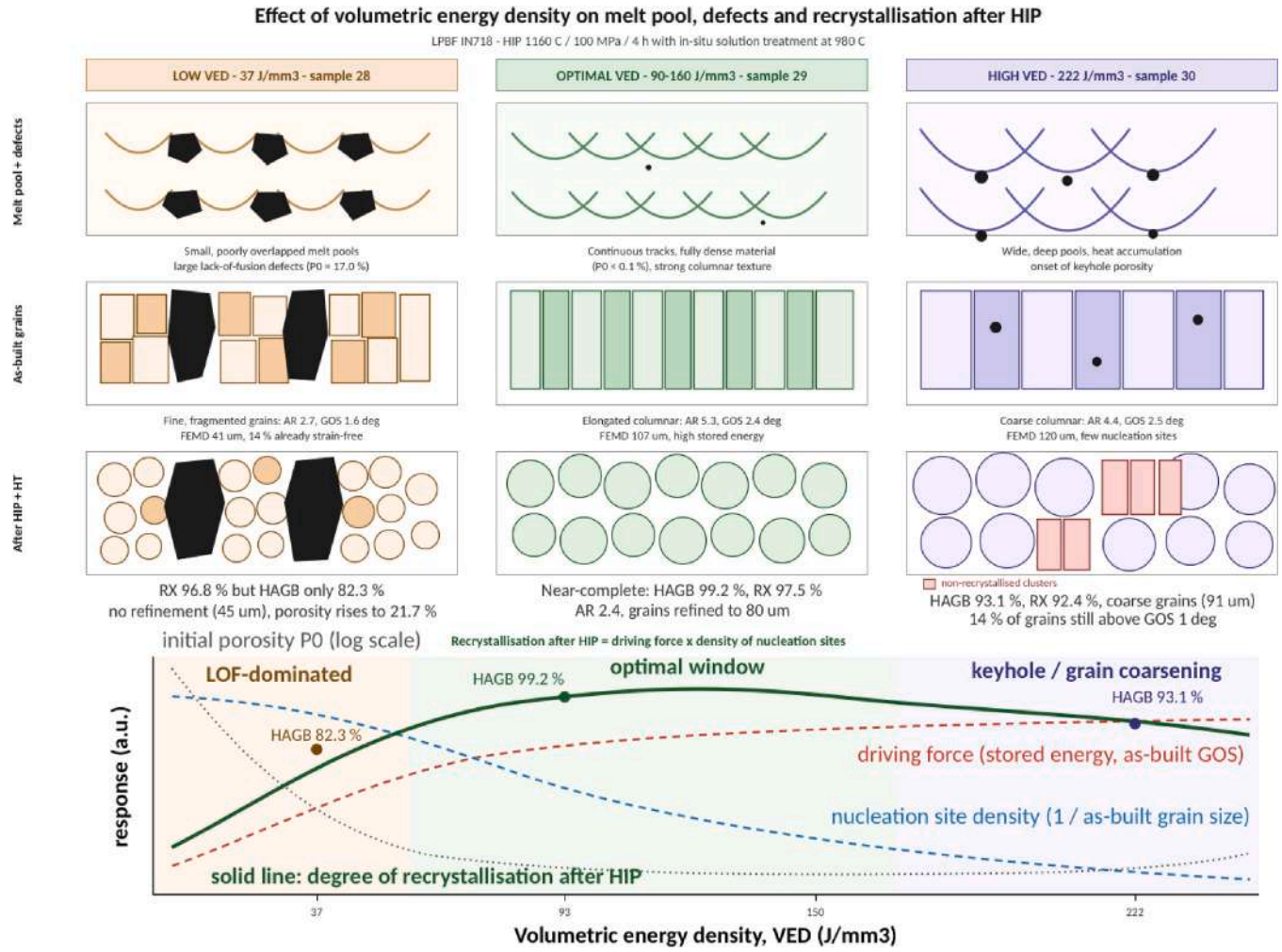

Fig. 13. Schematic representation of the effect of volumetric energy density on melt pool geometry, defect population and recrystallisation response after HIP in PBF-LB IN718. Low VED produces small, poorly overlapped melt pools, large lack-of-fusion defects and a weakly deformed as-built structure that only recovers during HIP; intermediate VED produces continuous, defect-free material with a highly deformed columnar structure that recrystallizes almost completely; high VED saturates the driving force while coarsening the grains and reintroducing keyhole porosity, leaving residual strained clusters after HIP. The bottom plot illustrates the resulting maximum in recrystallisation degree at intermediate VED as the product of a saturating driving force and a decreasing nucleation-site density (markers: measured post-HIP HAGB fractions for samples 28, 29 and 30).The curve is shown as a conceptual schematic linking these three measured conditions and does not represent a fitted or continuously validated relationship.

importance since it can be beneficial for creep resistance.

3.3. Nanoscale mechanical response to HIP + HT

The nanoindentation hardness maps presented in Fig. 14 provide spatially resolved insight into the local mechanical properties and heterogeneity introduced by the PBF-LB process and its evolution after HIP. Sample 29, in the pre-HIP condition depicted in Fig. 14(a), the hardness map exhibits a non-uniform spatial distribution with distinct high-hardness zones up to ~13 GPa, combined with softer regions in the range of ~6–8 GPa. This heterogeneity is directly correlated with the cellular-dendritic substructure characteristic of PBF-LB fabricated IN718, wherein Nb-rich cell boundaries and interdendritic regions, which are harder due to local laves phase precipitates and solute strengthening, alternate with the softer γ-matrix cell interiors. The corresponding reduced elastic modulus map also shows spatial variation in the range of approximately 200–400 GPa in the pre-HIP state, reflecting the anisotropic elastic response associated with the strong crystallographic texture typically generated during PBF-LB solidification, where grains preferentially grow along the ⟨001⟩ direction parallel to the build axis.

After HIP and heat treatment, the hardness map exhibits a markedly more spatially homogeneous distribution, with most values concentrated in a narrower range of approximately 10–14 GPa. This homogenization reflects the dissolution of Nb-rich laves phases at 1160°C, the redistribution of solute elements across the recrystallized grain structure, and the subsequent uniform reprecipitation of fine γ'' and γ' strengthening phases during double ageing. The elevated single nano hardness value is due to the MC carbides (NbC) present in the post-HIPped structure, with a value ranging from 20 to 24 GPa, which is documented in the literature [39]. The reduced modulus map similarly shows increased uniformity post-HIP except at the carbide phase.

The load-displacement curves shown in Fig. 14(b, d) provide complementary information about deformation mechanisms at the nanoscale. In the pre-HIP condition, the curves show a widespread in maximum penetration depth at the same peak load of 1 mN, ranging from approximately 45–75 nm. This spread reflects the spatial heterogeneity already discussed. In contrast, the post-HIP curves are considerably more clustered, with penetration depths converging toward a narrower range of approximately 45–55 nm except for the carbide phase, confirming that the microstructural homogenization achieved through HIP and heat treatment produces a more consistent local

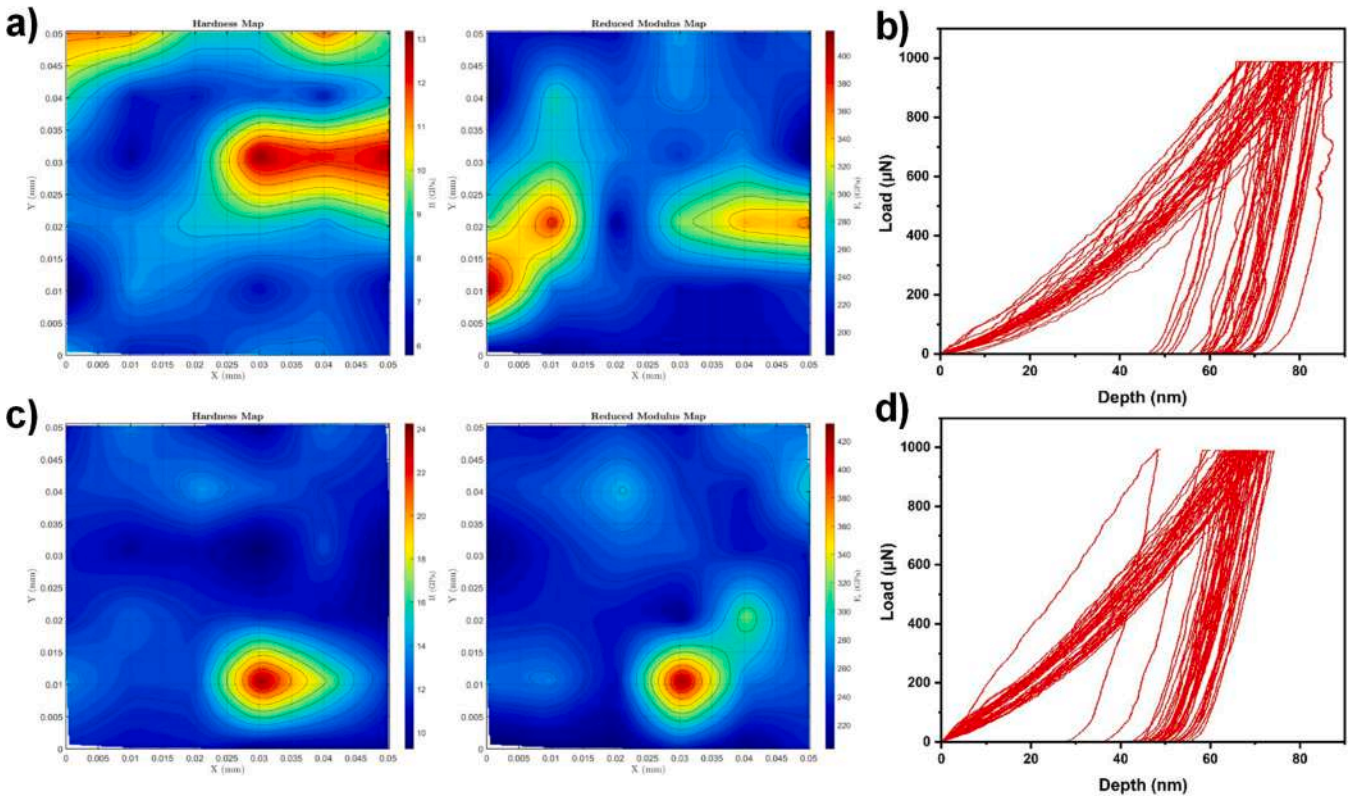

Fig. 14. Nanoindentation results from a 6 × 6 grid array showing (a) pre-HIP hardness map and modulus map, (b) pre-HIP load-displacement, (c) post-HIP hardness map and modulus map, and (d) post-HIP load-displacement curves.

mechanical response.

This homogenization is also reflected at the macroscale: Vickers hardness increased from approximately 320–385 HV1 before HIP to 500–540 HV1 after HIP and double ageing, with nearly uniform values across all thirty samples (Provided in the supplementary figures).

3.4. Evaluation of HIP effectiveness

The densification efficiency calculated for each sample provides a quantitative measure of HIP effectiveness. As shown in Fig. 15 the efficiency data separate into three behavioural regimes, connected by a transition band, according to the initial porosity of the specimen.

In the first regime ($P_o < \sim 0.1\%$), the absolute porosity reduction is smaller than 0.02 points and the calculated efficiency is dominated by measurement resolution rather than by closure behavior: because the denominator of Eq. 3 is very small, a change of one hundredth of a percentage point shifts the efficiency by roughly twenty points, which accounts for the wide scatter between 0% and 100% observed in this

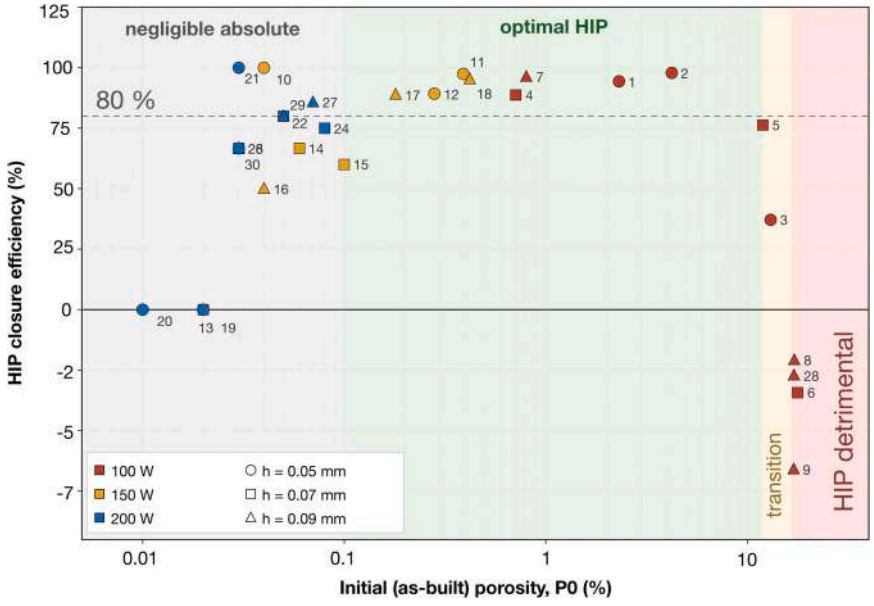

Fig. 15. Evolution of porosity before and after HIP vs efficiency across different samples.

range. The residual population in these specimens consists of sub-30 μm argon-filled spherical pores that neither close nor grow measurably. The absolute benefit of HIP is therefore marginal here and does not justify its cost, irrespective of the apparent efficiency value.

In the second and optimal regime ($\sim 0.1\% \leq P_o \leq \sim 10\%$), the efficiency is both high and consistent, ranging from 87% to 98% across samples 1, 2, 4, 7, 11, 12, 17 and 18. This range corresponds to specimens whose defect population is dominated by closed lack-of-fusion defects of intermediate size, which respond well to the combined creep, plastic collapse and diffusional bonding mechanisms activated at 1160 °C and 100 MPa. This is the window in which HIP delivers its full densification benefit.

Beyond ~10% the response degrades progressively rather than abruptly. Sample 5 ($P_o = 11.95\%$) and sample 3 ($P_o = 13.06\%$) still densify substantially, reaching final porosities of 2.83% and 8.21%, but their efficiencies fall to 76% and 37% respectively. This transition band indicates that an increasing fraction of the defect population has become interconnected and can no longer develop the pressure differential required for closure, while the remainder still responds normally.

In the third regime ($P_o \gtrsim 17\%$), the efficiency becomes negative for samples 6, 8, 9 and 28, indicating a net increase in porosity after processing. This is directly attributable to the open-pore network that forms once extensive LOF defects interconnect and breach the specimen surface, eliminating the pressure differential that drives HIP closure, and is compounded by the coalescence and gas-driven growth of the coarsest defects described in Section 3.1.1.

These results highlight that HIP is not universally effective for defect elimination in highly porous PBF-LB materials. Rather, its success is strongly governed by the initial pore characteristics, including morphology (spherical vs. lack-of-fusion), size distribution, and entrapped gas content, which collectively control the closure kinetics and final densification response.

4. Conclusions

This study systematically investigated the relationships among PBF-LB volumetric energy density, initial defect population, and HIP densification behaviour in Inconel 718 across a matrix of 30 specimens spanning nearly three orders of magnitude in initial porosity. The following principal conclusions are drawn:

- An approximately inverse monotonic relationship exists between VED and initial porosity. Below a critical threshold of ~60 J/mm^3 , porosity rises steeply due to the transition from stable conduction-mode melting to an unstable regime dominated by large irregular lack-of-fusion defects with aspect ratios exceeding 3:1. Above ~80 J/mm^3 , porosity remains below 5%, and further energy input offers diminishing densification returns while increasing keyhole pore risk. VED alone is not a sufficient descriptor of the defect state, however: at comparable energy density, specimens built at 100 W were systematically one to two orders of magnitude more porous than those built at 150 or 200 W (for example 2.31% at 111 J/mm^3 and 100 W against 0.28% at 100 J/mm^3 and 150 W). Below a minimum laser power, adequate melt pool overlap is not achieved regardless of scan speed and hatch spacing, so process qualification must be expressed in terms of the individual parameters and not of their lumped combination.
- HIP densification efficiency follows three regimes governed by initial porosity. For P_o below ~0.1%, the absolute reduction is smaller than 0.02 %age points and the residual population consists of sub-30 μm argon-filled spherical pores that neither close nor grow measurably; the calculated efficiency in this range is dominated by measurement resolution and the cost of HIP is not repaid. In the optimal window ($\sim 0.1\% \leq P_o \leq \sim 10\%$), closure efficiencies typically exceed 80% and reach 98%, driven by creep, plastic collapse and diffusional bonding of predominantly closed lack-of-fusion defects. Between ~10% and ~17% the response degrades progressively rather than abruptly (37–76% efficiency), and above ~17% it becomes negative: interconnected open-pore networks eliminate the pressure differential required for closure, and the final porosity reached 28.2% in the worst case, a relative increase of 66% over the as-built value. This is consistent with pore size distribution analysis, which reveals that mid-size defects in the 30–60 μm equivalent circular diameter range exhibit the highest HIP closure response (~50% count reduction), while the sub-30 μm gas-pore class shows only ~10% reduction due to inert gas entrapment. Critically, pores exceeding 300 μm increased in count by 125% after HIP, providing direct evidence of pore coalescence and argon-driven re-expansion during vacuum ageing in severely under-melted specimens.
- HIP at 1160 °C fully dissolved Nb-rich Laves phases and eliminated melt pool boundaries across all thirty samples regardless of initial porosity level, confirming complete microstructural homogenisation, and was accompanied by static recrystallisation from an elongated columnar to a predominantly equiaxed morphology. The degree of recrystallisation achieved during HIP appears to be non-monotonic with VED, based on the three conditions examined (37, 93 and 222 J/mm^3), passing through a maximum at intermediate energy density. At 37 J/mm^3 the weakly deformed as-built structure (GOS 1.6°) only recovers, reaching 96.8% recrystallised area but merely 82.3% high-angle boundary fraction and no grain refinement. At 93 J/mm^3 the combination of a highly deformed columnar structure and a defect-free matrix produces the most complete transformation (HAGB 99.2%, RX 97.5%, grain size refined from 107 to 80 μm). At 222 J/mm^3 the stored energy has already saturated while the as-built grains have coarsened, reducing the density of nucleation sites, so the transformation remains incomplete (HAGB 93.1%, 14% of grains above the 1° threshold) and the final structure is the coarsest and least equiaxed. The recrystallisation response can therefore be qualitatively rationalised as reflecting a saturating driving force and a decreasing nucleation-site density, both governed by VED, a pattern interpreted qualitatively based on the three measured conditions rather than a demonstrated quantitative relationship. The subsequent double-ageing cycle produced a uniform distribution of fine γ' and γ'' strengthening precipitates, with δ-phase and NbC carbides decorating grain boundaries, and nanoindentation mapping confirmed a marked reduction in spatial hardness heterogeneity relative to the as-built condition.
- The process window that minimises the pre-HIP defect population coincides with the one that maximises the microstructural benefit of the HIP cycle. Densification and microstructural homogenisation are therefore not independent post-processing objectives and should be qualified jointly.

This work identifies an optimal processing window for HIP post-processing of PBF-LB IN718 and establishes a practical pre-HIP porosity acceptance threshold beyond which HIP densification becomes ineffective or counterproductive, providing evidence-based criteria for the industrial qualification of additively manufactured nickel-based superalloy components, supporting cost-effectiveness and reliability for aerospace and energy applications.

CRediT authorship contribution statement

Jehanzaib Anwar: Writing – original draft, Investigation, Formal analysis, Data curation. **Emilio Bassini:** Writing – review & editing, Visualization, Validation, Supervision, Methodology. **Mattia Cannella:** Investigation, Formal analysis. **Giulio Marchese:** Resources, Investigation, Data curation. **Alessandra Martucci:** Investigation, Formal analysis. **Sara Biamino:** Writing – review & editing, Supervision, Resources. **Mariangela Lombardi:** Validation, Supervision, Resources. **Daniele Ugues:** Writing – review & editing, Supervision, Resources, Project administration, Conceptualization.

Declaration of Competing Interest

The authors declare the following financial interests/personal relationships which may be considered as potential competing interests: Jehanzaib Anwar reports financial support was provided by European Union. If there are other authors, they declare that they have no known competing financial interests or personal relationships that could have appeared to influence the work reported in this paper.

Acknowledgement

This work was funded by the European Union – Next Generation EU, Mission 4 Component 2 - ECS00000036 - CUP [E13B22000020001].

Appendix A. Supporting information

Supplementary data associated with this article can be found in the online version at doi:10.1016/j.jallcom.2026.191395.

Data Availability

Data is available from the corresponding author upon request.

References

[1] T. DebRoy, et al., Additive manufacturing of metallic components–process, structure and properties, Progress. Mater. Sci. 92 (2018) 112–224, https://doi.org/10.1016/j.pmatsci.2017.10.001.
[2] A. Mostafaei, et al., Additive manufacturing of nickel-based superalloys: A state-of-the-art review on process-structure-defect-property relationship, Progress. Mater. Sci. 136 (2023) 101108, https://doi.org/10.1016/j.pmatsci.2023.101108.
[3] W. Zheng, et al., Research on heat treatment of nickel–based superalloys by laser powder bed fusion: A review, J. Alloy. Compd. 1010 (2025) 177522, https://doi.org/10.1016/j.jallcom.2024.177522.
[4] C. Du, et al., Pore defects in Laser Powder Bed Fusion: Formation mechanism, control method, and perspectives, J. Alloy. Compd. 944 (2023) 169215, https://doi.org/10.1016/j.jallcom.2023.169215.
[5] D. Wang, et al., A review and a statistical analysis of porosity in metals additively manufactured by laser powder bed fusion, Opto-Electron. Adv. 5 (10) (2022) 210058, https://doi.org/10.29026/oea.2022.210058.
[6] S.A. Khairallah, et al., Laser powder-bed fusion additive manufacturing: Physics of complex melt flow and formation mechanisms of pores, spatter, and denudation zones, Acta Mater. 108 (2016) 36–45, https://doi.org/10.1016/j.actamat.2016.02.014.
[7] K. Amato, et al., Microstructures and mechanical behavior of Inconel 718 fabricated by selective laser melting, Acta Mater. 60 (5) (2012) 2229–2239, https://doi.org/10.1016/j.actamat.2011.12.032.
[8] D. Zhang, et al., Effect of standard heat treatment on the microstructure and mechanical properties of selective laser melting manufactured Inconel 718 superalloy, Mater. Sci. Eng. A 644 (2015) 32–40, https://doi.org/10.1016/j.msea.2015.06.021.
[9] S. Liu, et al., The effect of energy density on texture and mechanical anisotropy in selective laser melted Inconel 718, Mater. & Des. 191 (2020) 108642, https://doi.org/10.1016/j.matdes.2020.108642.
[10] V.P. Sabelkin, et al., Mitigation of anisotropic fatigue in nickel alloy 718 manufactured via selective laser melting, Mater. & Des. 182 (2019) 108095, https://doi.org/10.1016/j.matdes.2019.108095.
[11] J. Anwar, et al., A Review on Near Net Shape Hot Isostatic Pressing of Metallic Materials: For Industrial Applications, J. Mater. Res. Technol. (2026), https://doi.org/10.1016/j.jmrt.2026.03.210.
[12] S.-H. Chang, et al., Effects of temperature of HIP process on characteristics of Inconel 718 superalloy, Int. J. Cast. Met. Res. 19 (3) (2006) 175–180, https://doi.org/10.1179/136404606225023399.
[13] J. Yin, et al., The effects of hot isostatic pressing temperature and subsequent heat treatment on the microstructure and tensile properties of laser powder bed fused IN718 nickel-based superalloy, J. Alloy. Compd. 1020 (2025) 179407, https://doi.org/10.1016/j.jallcom.2025.179407.
[14] V.K. Singh, et al., Dissolution of the Laves phase and δ-precipitate formation mechanism in additively manufactured Inconel 718 during post printing heat treatments, Addit. Manuf. 81 (2024) 104021, https://doi.org/10.1016/j.addma.2024.104021.
[15] Y. Zhao, et al., Phase transformations during continuous cooling in Inconel 718 alloys manufactured by laser powder bed fusion and suction casting, Mater. Charact. 185 (2022) 111764, https://doi.org/10.1016/j.matchar.2022.111764.
[16] R. Ding, et al., Electron microscopy study of direct laser deposited IN718, Mater. Charact. 106 (2015) 324–337, https://doi.org/10.1016/j.matchar.2015.06.017.
[17] H. Guan, et al., Precipitation of δ phase in Inconel 718 superalloy: The role of grain boundary and plastic deformation, Mater. Today Commun. 36 (2023) 106582, https://doi.org/10.1016/j.mtcomm.2023.106582.
[18] J. Varela, et al., Performance characterization of laser powder bed fusion fabricated Inconel 718 treated with experimental hot isostatic processing cycles, J. Manuf. Mater. Process. 4 (3) (2020) 73, https://doi.org/10.3390/jmmp4030073.
[19] D. Sommer, et al., Fractographic Analysis and Fatigue Behavior of Additively Manufactured Ni-Superalloy Components with Post Processing Heat Treatment and Hot Isostatic Pressing. Adv. Eng. Mater. 27 (12) (2025) 2500078 https://doi.org/10.1002/adem.202500078.
[20] H. Atkinson, S. Davies, Fundamental aspects of hot isostatic pressing: An overview, Metall. Mater. Trans. A 31 (12) (2000) 2981–3000, https://doi.org/10.1007/s11661-000-0078-2.
[21] K. Qian, et al., Solubility of Nitrogen in Liquid Ni, Ni–Nb, Ni–Cr–Nb, Ni–Fe–Nb, and Ni–Cr–Fe–Nb Systems, ISIJ Int. 59 (12) (2019) 2220–2227, https://doi.org/10.2355/isijinternational.ISIJINT-2019-187.
[22] A. Kaletsch, et al., Influence of high initial porosity introduced by laser powder bed fusion on the fatigue strength of Inconel 718 after post-processing with hot isostatic pressing, Addit. Manuf. 47 (2021) 102331, https://doi.org/10.1016/j.addma.2021.102331.
[23] W. Tillmann, et al., Hot isostatic pressing of IN718 components manufactured by selective laser melting, Addit. Manuf. 13 (2017) 93–102, https://doi.org/10.1016/j.addma.2016.11.006.
[24] P. Kasay, et al., Hot Isostatic Pressing of Additive Specimens, Grown from IN718 Alloy Powder Obtained by Gas Atomization, Strength. Mater. 56 (4) (2024) 722–734, https://doi.org/10.1007/s11223-024-00686-w.
[25] H. Javidrad, et al., Effect of heat treatment and hot isostatic pressing on the microstructure and mechanical properties of the directed energy deposition IN738LC and IN718: A comparative study, Mater. Charact. 227 (2025) 115279, https://doi.org/10.1016/j.matchar.2025.115279.
[26] K. Miao, et al., Mechanisms of heat-treatment-induced cracking in additively manufactured IN738 alloy, Materials 16 (23) (2023) 7316, https://doi.org/10.3390/ma16237316.
[27] A. Rezaei, et al., Contribution of hot isostatic pressing on densification, microstructure evolution, and mechanical anisotropy of additively manufactured IN718 Ni-based superalloy, Materials Science Engineering A 823 (2021) 141721, https://doi.org/10.1016/j.msea.2021.141721.
[28] A. International, Standard Specification for Additive Manufacturing Nickel Alloy (UNS N07718) with Powder Bed Fusion, ASTM International, West Conshohocken, PA, 2014.
[29] T. Huynh, et al., Microstructural development in Inconel 718 nickel-based superalloy additively manufactured by laser powder bed fusion, Metallogr. Microstruct. Anal. 11 (1) (2022) 88–107, https://doi.org/10.1007/s13632-021-00811-0.
[30] G. de Leon Nope, et al., Study of volumetric energy density limitations on the IN718 mesostructure and microstructure in laser powder bed fusion process, J. Manuf. Process. 64 (2021) 1261–1272, https://doi.org/10.1016/j.jmapro.2021.02.043.
[31] N. Nudelis, P. Mayr, Pore tracing in additive manufactured and hot isostatic pressed components, J. Mater. Sci. 58 (35) (2023) 14245–14253, https://doi.org/10.1007/s10853-023-08907-4.
[32] A. Paraschiv, et al., The influence of laser defocusing in selective laser melted in 625, Materials 14 (13) (2021) 3447, https://doi.org/10.3390/ma14133447.
[33] L. Scime, J. Beuth, Melt pool geometry and morphology variability for the Inconel 718 alloy in a laser powder bed fusion additive manufacturing process, Addit. Manuf. 29 (2019) 100830, https://doi.org/10.1016/j.addma.2019.100830.
[34] E.M. Fayed, et al., Influence of homogenization and solution treatments time on the microstructure and hardness of Inconel 718 fabricated by laser powder bed fusion process, Materials 13 (11) (2020) 2574, https://doi.org/10.3390/ma13112574.
[35] S. Sui, et al., Laves phase tuning for enhancing high temperature mechanical property improvement in laser directed energy deposited Inconel 718, Compos. Part B Eng. 215 (2021) 108819, https://doi.org/10.1016/j.compositesb.2021.108819.
[36] J. Xu, et al., Effect of heat treatment temperature on the microstructural evolution of CM247LC superalloy by laser powder bed fusion, Mater. Charact. 185 (2022) 111742, https://doi.org/10.1016/j.matchar.2022.111742.
[37] D.H. Son, et al., Effect of laser power on the recrystallization temperature of an additively manufactured IN718, Metals 13 (8) (2023) 1355, https://doi.org/10.3390/met13081355.
[38] F. Deirmina, et al., Effect of layer thickness, and laser energy density on the recrystallization behavior of additively manufactured Hastelloy X by laser powder bed fusion, Addit. Manuf. Lett. 7 (2023) 100182, https://doi.org/10.1016/j.addlet.2023.100182.
[39] A. Orozco-Caballero, et al., High-throughput nanoindentation mapping of cast IN718 nickel-based superalloys: influence of the Nb concentration, J. Mater. Res. 36 (11) (2021) 2213–2222, https://doi.org/10.1557/s43578-021-00133-5.